Structural damage detection using Bayesian inference and seismic interferometry

Received ; | Revised ; | Accepted

DOI: xxx/xxxx

ARTICLE TYPE

Structural damage detection using Bayesian inference and seismic interferometry

Murat Uzun[1] | Hao Sun[1,2] | Dirk Smit[3] | Oral Büyüköztürk[1]

[1]Department of Civil and Environmental Engineering, MIT, Cambridge, MA 02139, USA
[2]Department of Civil and Environmental Engineering, Northeasthern University, Boston, MA 02115, USA
[3]Shell Global Solutions International, Shell, The Hague, 162, 2501 AN, The Netherlands

Correspondence
Oral Büyüköztürk, Department of Civil and Environmental Engineering, MIT, Cambridge, MA 02139, USA
Email: obuyuk@mit.edu

Hao Sun, Department of Civil and Environmental Engineering, Northeasthern University, Boston, MA 02115
Email: h.sun@northeastern.edu

Summary

We present a computational methodology for structural identification and damage detection via linking the concepts of seismic interferometry and Bayesian inference. A deconvolution-based seismic interferometry approach is employed to obtain the waveforms that represent the impulse response functions (IRFs) with respect to a reference excitation source. Using the deconvolved waveforms, we study the following two different damage detection methods that utilize shear wave velocity variations: the arrival picking method and the stretching method. We show that variations in the shear wave velocities can be used for qualitative damage detection, and that velocity reduction is more evident for more severely damaged states. Secondly, a hierarchical Bayesian inference framework is used to update a finite element model by minimizing the gap between the predicted and the extracted time histories of the IRFs. Through comparison of the model parameter distributions of the damaged structure with the updated baseline model, we demonstrate that damage localization and quantification is possible. The performance of the proposed approach is verified through two shake table test structures. Results indicate that the proposed framework is promising for monitoring structural systems, which allows for non-invasive determination of structural parameters.

KEYWORDS:
Structural health monitoring, seismic interferometry; probabilistic model updating; bayesian inference; stretching method; structural identification; damage detection

1 | INTRODUCTION

Vibration-based damage identification methodologies, as a major branch in structural health monitoring (SHM), generally track the changes in dynamical features of a structural system such as natural frequencies, mode shapes, structural damping values, mode shape curvatures, modal strain energies, etc.[1–6]. Tremendous efforts have been made over the last two decades[7–13]. Recently, wave propagation-based approaches have also started to gain attention. Considering the physics behind the earthquake (EQ) response of a structure, actual seismic waves that are initiated due to a fault rupture reach the surface, thereafter propagate into the structure, causing structural vibrations[14–17]. As the changes in the wave travel time between two observation locations only depends on the changes in the physical properties of the connecting medium, wave methods are considered to be more sensitive to local changes[18–20]. However, wave-based monitoring methods generally assume 1D wave propagation within

[0]**Abbreviations:** IRF, impulse-response functions; FEM, finite element model

the building and have its own limitations and challenges[21]. For more in depth damage diagnosis, these macro-scale dynamical features can be further coupled with computational models through successful implementation of finite element model (FEM) updating schemes when design information about the structure is available (e.g., materials, topology, connection types, etc.)[22,23]. Considering the required modeling assumptions and the inherent measurement noise, the Bayesian model updating framework offers a robust and rigorous basis for structural condition assessment and consequent reliability evaluation[24–34]. Essentially, it specifies how to characterize and quantify the uncertainty of the models as well as the predictions against the measurements[35]. Even though the framework is conceptually straightforward, learning reliable models from the data leads to computational challenges (e.g., marginalizing).

Deconvolution-based seismic interferometry, proposed by Snieder and Safak[36], is one of the first techniques that employs wave propagation as a basis for monitoring structures. It is a method to extract the Green's function of the medium, which is the impulse response solution of the differential equation that defines the dynamics of the system of interest. Essentially, deconvolving the recorded signal on receivers of interest (e.g., acceleration-time series of the i^{th} story) with respect to signal recorded on a reference receiver (e.g., acceleration-time series of ground story) yields waveforms consisting of wave propagation information given a virtual impulse input at the reference, namely, the impulse-response functions (IRFs). This technique has been proven to be successful and improved by many other researchers in the field[37–39]. Further details are provided in Section 2.

In this paper, we extend the framework previously presented by Sun et al.[39], where interferometric data analytics are linked with Bayesian inference, to establish a more holistic approach for identification of structural damage. In particular, we address the problem by utilizing earthquake response data, aiming to achieve damage detection as well as localization and quantification. Firstly, using earthquake response measurements, we apply the deconvolution interferometry technique to extract the IRFs of the structure of interest. These waveforms are analyzed to form a qualitative damage detection strategy, given that the response data from the undamaged case is present. We test two different damage detection methods that use shear wave velocity variations: (1) the arrival picking method and (2) the stretching method. It is noted that the stretching method produces higher sensitivity for damage detection. Then, we perform the finite element model calibration, applying the hierarchical Bayesian framework. The extracted time-histories of IRFs are utilized to learn the physical parameters of a suitable FEM. We employ Markov Chain Monte Carlo (MCMC) sampling in order to obtain the posterior probability distributions (PDFs) of the model parameters. Uncertainty quantification of model parameters (e.g., lateral story-stiffness values) is realized inherently through the Bayesian inference framework. We demonstrate that the damage quantification is possible through comparing the model parameter distributions of the damage state with the baseline parameter distributions of the "intact" (referred to healthy or undamaged state) structure. It should be noted that the work by Sun et al.[39] has only focused on updating the baseline model using ambient measurements. In this paper we tried to fill the research gap by investigating damage detection and localization capabilities and limitations of the framework which has not been previously addressed.

This paper is structured as follows. Section 2 describes the deconvolution-based seismic interferometry approach. We elaborate on the dynamic characteristics of a structure acquired through seismic interferometry, i.e., shear-wave velocities and damping ratios. Section 3 introduces the Bayesian model updating framework. In Section 4, we first evaluate the structural identification performance of the proposed approach on experimental shake-table data of a scaled steel structure with different damage scenarios (induced via bolt loosening at the floor joints) in order to validate the proposed methodology. We further deploy our framework on a full-scale 7-story reinforced concrete building slice, which was progressively damaged via previously recorded historical earthquake records utilizing the University of California, San Diego Network for Earthquake Engineering Simulations (UCSD-NEES) shake-table. Finally, Section 5 discusses the implications of the results and scope for further research.

2 | EXTRACTING STRUCTURAL WAVES

In the area of vibration-based SHM, the fundamental objective is to determine the intrinsic changes in a structure based on its measured dynamic response. In this study, we extract the structural waves, which are isolated from the soil-structure interaction, applying the deconvolution-based seismic interferometry technique. The extracted waves are also called impulse response functions (IRFs) which can be used to identify dynamical parameters, such as shear wave travel velocities, modal frequencies, mode shapes and intrinsic attenuation (damping) values. Note that deconvolved waveforms satisfy the same wave equation as the original physical system with different boundary conditions[40].We extract the IRFs by deconvolving the recorded acceleration

time series of a structure with respect to a reference record of choice. The deconvolution operation can be formulated as [36,39]

$$S(z,t) = F^{-1}\left(\frac{y(z,w)y^*(z_{ref},w)}{|y^*(z_{ref},w)|^2+\delta}\right) \tag{1}$$

where $S(z,t)$ is the IRF at z; $y(z,w)$ is the frequency domain quantify of the response measurement at z; $|y^*(z_{ref},w)|^2$ is the power spectrum of y_{ref}; w is angular frequency; t is time; y_{ref} is the reference level of the building; $*$ denotes the complex conjugate; δ is a stabilizing parameter (water-level parameter[36], e.g., 0.1%); and F^{-1} denotes the inverse Fourier transform. The stabilizing parameter, ϵ, is conventionally set to some fixed/pre-determined percentile of the power of the reference signal, $y(z_{ref},t)$, and it is essential to regularize the operation. $S(z,t)$ physically represents the response of the structural system at height z to a unit impulse at the reference level z_{ref}. This reconstructed structural system has fixed boundary conditions at height z_{ref}. Therefore, the extracted IRFs through the height of the building, show how the virtual pulse (or disturbance) propagates through the system. These functions represent the input-output relationships and provide a complete picture of the characteristics of linear time invariant (LTI) systems. It is noted that an IRF is the intrinsic property of a linear and undamaged system. Considering civil structures under earthquake shaking, the deconvolution operation is done with respect to the ground-level record, yields causal waveforms, since the physical input (i.e., incoming seismic waves) to the structural system is at ground level. This means that the motion of the building response follows the base excitation in time. Selecting another reference where there is no real source, e.g., receiver at the top floor (in the presence of an earthquake), yields waveforms consisting of both causal and acausal parts. The down-going acausal wave can be physically interpreted as the up-going wave that enters the structural system prior to shaking at the top floor. Nakata et al.[19] have argued that selecting different reference receivers at different stories could be used to investigate the local damages as the deconvolution operation yields a cut-off building system.

2.1 | Estimating wave velocity variations via a stretching technique

Shear wave velocity can be estimated based on the extracted IRFs by tracing the first crest of the shear wave pulse that travels upwards from the reference source location. Therefore, by the arrival picking method (APM), the wave velocity is determined by fitting a linear line, in a least-square sense, to wave travel times (time of arrivals of the first peaks) and wave travel distances (story elevations). The slope of the fitted line corresponds to the shear-wave velocity of the wave that propagates within the structure. Note that, this method can be used when deconvolution is calculated with a virtual source at the roof level as well. For a structure that is excited by an earthquake, Snieder and Safak[36] showed that selecting the roof level as the reference yields one acasual up-going wave and one causal down-going wave. In line with their work, we show that the obtained deconvolved waves with respect to the recorded signal at the ground level and the top level of a structure provide complementary information.

By the stretching method (SM), instead of calculating the absolute wave velocity, the relative velocity variations are calculated by assuming that a homogeneous velocity change that takes place in the medium. In seismology, this method is mainly used for measuring the perturbations of coda-waves. The underlying mathematical framework can be found in [41]. Essentially, by stretching the current wave, that travels in the perturbed medium, along the time axis to maximize its correlation to a reference wave, an optimal stretching coefficient can be determined. This coefficient, ϵ, represents the velocity variation of the current waveform with respect to the reference wave velocity, as expressed in Equation (3). First, we express the stretched waveform as

$$f_\epsilon(t) = f^{cur}(t(1-\varepsilon)) \tag{2}$$

where, $f^{cur}(t)$ denotes the current wave (e.g., damaged IRF) and $f_\epsilon(t)$ denotes the stretched wave. Then the correlation coefficient $C(\varepsilon)$ can be calculated as follows

$$C(\epsilon) = \frac{\int_{t_1}^{t_2} f_\epsilon(t) f^{ref}(t)dt}{\sqrt{\left(\int_{t_1}^{t_2} f_\epsilon(t)^2 dt\right)\left(\int_{t_1}^{t_2} f^{ref}(t)^2 dt\right)}} \tag{3}$$

where $f^{ref}(t)$ is the reference trace (e.g., undamaged IRF), and t_1 and t_2 represents the starting and ending points of the time series of interest along the waveform. We find the maximum correlation coefficients and the respective stretching coefficients by grid search for each measurement channel[42]. Note that, since we are working with discrete-time signals, after the stretching operation, interpolation is necessary to directly calculate the inner product of the stretched and reference signals. Estimated values for the maximum correlation coefficients depend on the selected time periods of interest along the waves. For example, in the SHM context, the later part of the deconvolved waves, with the excitation source at the ground level, predominantly contain

the fundamental mode, as its attenuation is more gradual. The initial part of the waves, however, contain superposition of many overtones. Note that the SM can also be applied to estimate the frequency series from long-term SHM data[43].

2.2 | Damping parameter estimation

There exist many damping models (e.g., non-viscous), any of which could be favored depending on the nature of the engineering problem[44]. Assuming a linear system, each harmonic's corresponding damping ratio can be calculated by tracing the amplitude decay with time. In this study, we calculate the damping ratios by fitting linear lines to the envelope of the natural logarithm of the IRFs, which are band-pass filtered around the resonant frequencies within the half-power bandwidth[36,37,39].

$$\xi_r = \frac{1}{N_0 \omega_r} \sum_{i=1}^{N_0} |\mu_i| \tag{4}$$

In Equation (4), μ_i is the slope of the envelope, ω_r is the r^{th} resonance frequency, N_0 is the number of observations (e.g., observed number of stories), and i is the observation location/story of interest. Knowing the damping ratios, the quality factor, $\mathbf{Q}$, of the building can be estimated. For homogenous materials, the quality factor does not typically depend on the frequency of the oscillation[45,46].

Using Rayleigh's assumption[47], the proportional damping matrix, $\mathbf{C}$, can be assembled as a linear combination of the stiffness matrix, $\mathbf{K}$, and the mass matrix, $\mathbf{M}$. The proportionality constants can be found using any two damping ratio estimates. Note that, this assumption yields classical normal modes for linear dynamical systems, and performs well enough with experimental data[48]. Therefore, in this study, we estimate the damping ratios of the first two resonant peaks of the frequency response functions of the extracted waves using Equation (4) and use them to determine the Rayleigh damping matrix.

3 | PROBABILISTIC MODEL UPDATING

3.1 | Bayesian Framework

Time-histories of the outputs of a system can be used to estimate the physical parameters of a representative finite-element model by making use of probabilistic model updating schemes. In our case, the fundamental aim of structural model updating is to minimize the gap between the predicted and the measured IRFs by quantifying posterior probability distributions of a set of model parameters, $\boldsymbol{\theta} \in \mathbb{R}^{N_\theta \times 1}$. Herein, we consider a linear shear beam model with N_θ degrees-of-freedoms (DOFs), which is suitable to capture the dynamics of mid-rise and high-rise buildings. This model can be portrayed as a chain of lumped masses that are consecutively connected by springs and dashpots. Note that, this type of arrangement leads into band-limited structural matrices. The mass matrix, $\mathbf{M} \in \mathbb{R}^{N_\theta \times N_\theta}$, is assumed to be fixed and known as a priori. As previously mentioned in Section 2.2, we construct our proportional damping matrix, $\mathbf{C}$, by using Equation (4). We parameterize our stiffness matrix, $\mathbf{K} \in \mathbb{R}^{N_\theta \times N_\theta}$ by $\theta = [\theta_1, \theta_2, \dots, \theta_{N_\theta}]$, where each θ_i represents i^{th} story's lateral stiffness in the shaking direction.

Using the hierarchical Bayesian inference[39,49–52], we formulate the model updating problem as follows

$$p(\boldsymbol{\theta}, \sigma^2 | \mathcal{D}) \propto p(\mathcal{D} | \boldsymbol{\theta}, \sigma^2) p(\boldsymbol{\theta}) p(\sigma^2) \tag{5}$$

where $p(\boldsymbol{\theta}, \sigma^2 | \mathcal{D})$ denotes the posterior probability density function (PDF) of unknown parameters $\{\boldsymbol{\theta}, \sigma^2\}$; $p(\mathcal{D} | \boldsymbol{\theta}, \sigma^2)$ is the likelihood function conditional on the measurements data $\mathcal{D}$ (e.g., the extracted IRFs); $p(\boldsymbol{\theta})$ and $p(\sigma^2)$ are the prior PDFs. In particular, the likelihood function and the prior PDFs can be written as

$$p(\mathcal{D} | \boldsymbol{\theta}, \sigma^2) = \left(\frac{1}{2\pi\sigma^2} \right)^{\frac{N_o N_t}{2}} \exp\left\{ -\frac{J(\boldsymbol{\theta})}{2\sigma^2} \right\} \tag{6}$$

$$p(\boldsymbol{\theta}) = \frac{1}{\sqrt{|2\pi \boldsymbol{\Sigma}_{\boldsymbol{\theta}}|}} \exp\left\{ -\frac{1}{2} (\boldsymbol{\theta} - \boldsymbol{\theta}_{\mathbf{0}})^T \boldsymbol{\Sigma}_{\boldsymbol{\theta}}^{-1} (\boldsymbol{\theta} - \boldsymbol{\theta}_{\mathbf{0}}) \right\} \tag{7}$$

$$p(\sigma^2) = p(\sigma^2 | \alpha, \beta) = \frac{\beta^\alpha}{\Gamma(\alpha)} \left(\frac{1}{\sigma^2} \right)^{\alpha+1} \exp\left\{ -\frac{\beta}{\sigma^2} \right\} \tag{8}$$

where $J(\boldsymbol{\theta}) = \sum_{j=1}^{N_t} \|\hat{\mathbf{S}}(\boldsymbol{\theta}, t_j) - \mathbf{S}(t_j)\|_2^2$ is the *goodness-of-fit* function; $\mathbf{S}(t_j) \in \mathbb{R}^{N_o \times 1}$ denotes the IRFs at time t_j extracted from

the measurement data ($j = 1, 2, ..., N_t$), while $\hat{\mathbf{S}}(t_j) \in \mathbb{R}^{N_o \times 1}$ is the model predicted IRFs; N_o is the total number of channels of measurement; $\|.\|$ stands for the Euclidean norm; σ^2 denotes the prediction error variance, which is also considered as an unknown parameter and should be estimated right along with the model parameters. The prior PDF of the model parameters in Equation (7) is modeled by the multivariate Gaussian distribution, $\mathcal{N}(\boldsymbol{\theta_0}, \boldsymbol{\Sigma_\theta})$, where the choice of mean parameter vector $\boldsymbol{\theta}_0 \in \mathbb{R}^{N_\theta \times 1}$ and the covariance matrix $\boldsymbol{\Sigma}_{\boldsymbol{\theta}} \in \mathbb{R}^{N_\theta \times N_\theta}$ are user defined. Here, mean parameter vector, $\boldsymbol{\theta}_0$ is given by, $\boldsymbol{\theta}_0 = [\overline{\theta}_1, \overline{\theta}_2, \dots, \overline{\theta}_{N_\theta}]^T$ where, $\overline{\theta}_i$ is the mean value of the respective parameter (e.g., $\overline{\theta}_2$ is the mean lateral stiffness of the second story). Since the prediction error variance σ^2 is always positive, utilizing the conjugacy concept, we model its prior PDF $p(\sigma^2)$ in Equation (8) as an inverse gamma distribution, $p(\sigma^2) \sim IG(\alpha, \beta)$, with positive constant hyper-parameters α and β, which are chosen extremely small to retain a non-informative prior (e.g., $\alpha = 10^{-3}$, $\beta = 10^{-6}$).

Substituting the likelihood function and the priors, Equations (6), (7), and (8) into Equation (5), the final form of the augmented multivariate posterior PDF can be observed as follows

$$p(\boldsymbol{\theta}, \sigma^2|\mathcal{D}) \propto \left(\frac{1}{\sigma^2}\right)^{\frac{N_0 N_t}{2}+\alpha+1} \exp\left\{-\frac{1}{\sigma^2}\left(\frac{J(\boldsymbol{\theta})}{2}+\beta\right) - \frac{1}{2}(\boldsymbol{\theta}-\boldsymbol{\theta_0})^T \boldsymbol{\Sigma}_{\boldsymbol{\theta}}^{-1}(\boldsymbol{\theta}-\boldsymbol{\theta_0})\right\} \tag{9}$$

Note that $p(\sigma^2|\boldsymbol{\theta}, \mathcal{D})$ is analytically obtainable, given the model parameter vector $\boldsymbol{\theta}$, and it follows an inverse Gamma distribution, $IG(a, b)$, (see Equation (8)) according to

$$p(\sigma^2|\boldsymbol{\theta}, \mathcal{D}) \propto \left(\frac{1}{\sigma^2}\right)^{\frac{N_0 N_t}{2}+\alpha+1} \exp\left\{-\frac{1}{\sigma^2}\left(\frac{J(\boldsymbol{\theta})}{2}+\beta\right)\right\} \tag{10}$$

where the parameters $a = (N_0 N_t)/2 + \alpha$ and $b = J(\boldsymbol{\theta})/2 + \beta$. Utilizing Equation (10) facilitates our sampling procedure, since most statistical toolboxes provide built-in sampling implementation for inverse Gamma distribution. As the implicit analytical expression for the posterior distribution in Equation (9) requires multi-dimensional integrals of a very complicated expression, in order to calculate the desired marginal parameter distributions, the Markov chain Monte Carlo method is employed. Details regarding the utilized MCMC sampler are described in the following section. On the other hand, for the prediction error variance, samples can be drawn from the expression shown in Equation (10) for a given $\boldsymbol{\theta}$. Note that utilizing the Markov Chains that effectively represent the multivariate posterior distribution, $p(\boldsymbol{\theta}, \sigma^2|\mathcal{D})$, one can compute the maximum a-posteriori estimate (MAP) of each model parameter along with the posterior covariance matrix. The latter provides an insight about the correlation in between model parameters and a quantitative measure of uncertainty related to parameter vector $\boldsymbol{\theta}$[53].

3.2 | Sampling Marginal Posterior PDFs

The Bayesian learning schemes are known to yield complicated high-dimensional posterior distributions. Therefore, drawing independent samples utilizing typical Monte Carlo methods, such as importance sampling or rejection sampling, is difficult as they require proposal distributions that are similar to the distribution we want to sample. On the other hand, methods based on the Markov chains, such as Gibbs sampling[54], Metropolis-Hasting algorithm, Hamiltonian Monte Carlo, and slice sampling, effectively allow us to draw dependent samples that eventually represent the target posterior distributions[55]. The stated simulation procedures are named as MCMC methods. In this study, to draw samples that effectively represent the derived posterior $p(\boldsymbol{\theta}, \sigma^2|\mathcal{D})$ in Equation (9), we implement an MCMC sampler that is described as follows. Markov chains are created employing the Metropolis-Hasting algorithm, where we update our state vector $\boldsymbol{\theta}$ systematically, one by one[56]. We use Cauchy distribution (CD) as our proposal distribution, with a predefined width/step size κ. For each Markov step, CD is centered on the current value of the state component $\theta_k^{(i-1)}$. If the candidate step resides in a higher probability density region, then it is accepted. If the chain moves into a lower probability density region, however, the candidate state is accepted according to a Bernoulli trial. The value of κ is determined considering the computation time and the ratio between acceptance and rejection through several simulations. Note that we use the same step size, κ, for every model parameter. We initialize the sampler by specifying the chain length, burn-in period length, beginning state of the parameter vector (starting point of the random walk), prior distributions, step size κ, the hyper-parameters (i.e., α, β) of the IG distribution, the mass matrix, $\mathbf{M}$, the Rayleigh coefficients α_R and β_R and the extracted IRFs $S(z, t)$. In every iteration, the value of prediction error variance, which will be used in the next iteration, is sampled following the Equation (10). For the same chain index, constant σ^2 is used. This algorithm outputs the structural model parameter samples (i.e., marginal posteriors) together with prediction error variance samples. Since the algorithm is initialized with a user-defined (mostly arbitrary) state, the samples from the non-stationary initial part of the corresponding chain

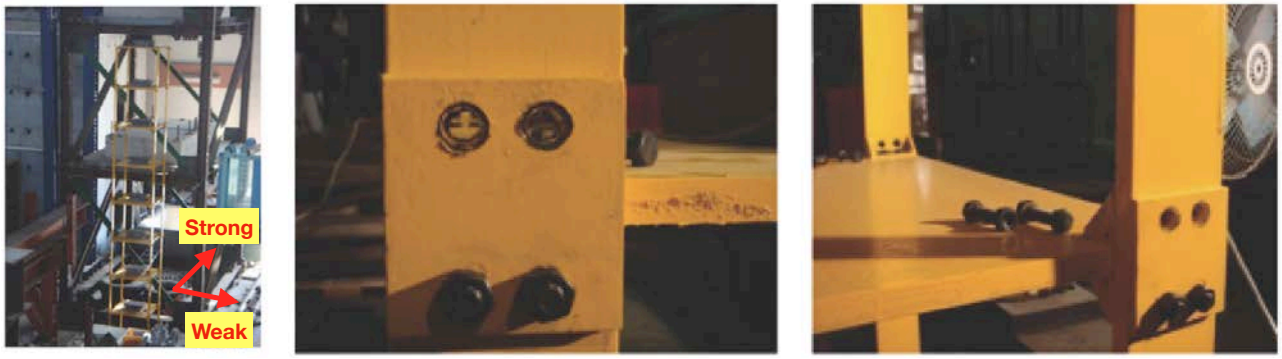

FIGURE 1 8-story experimental structure and the induced damage due to the loose bolt.

are discarded. The part of the chain that is used to describe the target distribution is called the 'retained period', whereas the discarded portion is called the 'burn-in'period. Through a detailed inspection of the histograms of marginal posteriors, quantitative damage detection is achievable.

4 | VALIDATION

4.1 | Experimental Case Study 1: Scaled 8-story Steel Structure

We initially evaluate our procedure utilizing measurements from shake-table tests which were operated by the National Center for Research on Earthquake Engineering (NCREE), in Taiwan. The structure has a story height of 33 cm and accommodates steel (ASTM A36) columns that are connected to the slabs with bolts as shown in Figure 1. Each slab has the dimension of 43×45cm and an additional 50 kg mass was installed at the center. The test structure is fixed to the shake table. The acceleration measurements were carried out along the weak direction (see Figure 1) with a sampling rate of 200 Hz. Different damage scenarios were tested by loosening the bolts at the floor joints, as it is illustrated in Figure 1. In our study, we use the dataset in which the base excitation was rescaled to match the ChiChi earthquake with a peak ground acceleration (PGA) value of $0.07g$. Note that, other tests with different earthquake inputs, e.g., Kobe, El-Centro, were also performed and we use them to validate the learned structural FEM. Recorded acceleration response of the test structure is shown in Figure 2(a). In particular, we worked on damaged scenarios where the bolt loosening occurred at the connection between the first and second stories, denoted with D(1), and between the lowest three stories, denoted with D(2). In particular, for each damage scenario, two out of four bolts are removed for each column as illustrated in Figure 1. Note that the intact/baseline state is hereafter denoted by D(0).

IRF estimates of state D(0) are shown in Figure 2(b) and Figure 2(c). By plotting the IRFs vs. the structural elevation, both up-going and down-going waves can be observed. Using the recorded base excitation as the reference, it is shown that the initial parts of the deconvolved waves consist of many overtones i.e., superposition of traveling waves whereas the later parts mostly contain the fundamental mode of the test structure since the higher modes die out more quickly. In order to calculate the damping ratios through linear curve fitting using Equation (4), we first compute the PSD estimate of the extracted IRFs (see Figure 3(a)). Utilizing the band-pass filtered IRF envelopes, we compute the slopes of the fitted lines and calculate the damping ratios respectively as $\xi_1 = 2.3\%$ and $\xi_2 = 2.4\%$ (see Figure 3(b-c)). Note that, these damping ratios are used to construct the damping matrix, $\mathbf{C}$, of the structural FEM. We then investigate the resulting waveforms by observing the wave velocity variations.

With the SM, the stretching coefficient represents the relative velocity variation, and therefore, we first sample 2000 stretching coefficients between -40% and 40%, then we calculate the correlation coefficient of each stretched waveform with its reference trace. It is noted that the reference trace for each story is selected as the initial three second piece of the corresponding stories' intact IRF i.e., from D(0). For example, Figure 4 demonstrates the deconvolved waves before and after stretching operation. It can be seen that the maximum correlation is achieved through contracting the IRFs from the damaged structure and the stretched waves matches the reference waves quite well. Nevertheless, it should be noted that, though the IRFs for the damage case are not simply the stretched version of the undamaged one (as shown in Figure 4), the SM can capture well the phase differences which are highly related to structural stiffness changes. In the APM, wave velocity is determined by tracking the arrival time of the first peak to each story. Figure 5(a-b) presents the correlation between the severity of the damage and the estimated shear

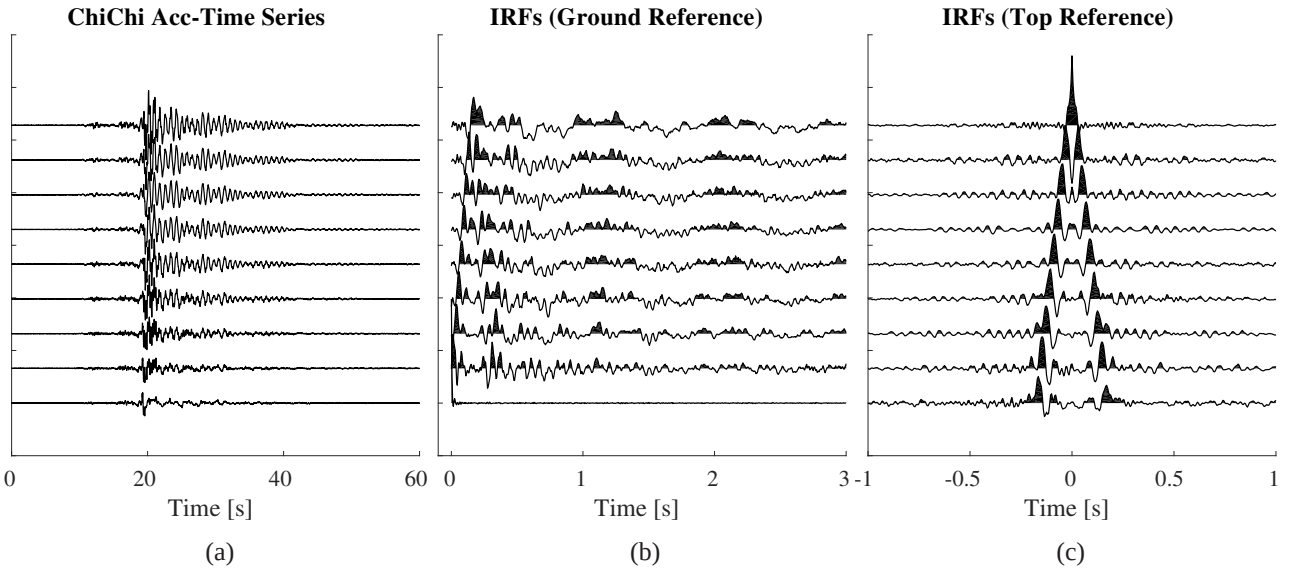

FIGURE 2 From left to right: (a) recorded ChiChi earthquake response of the experimental test structure; (b) deconvolved waves using recorded basement time-series (i.e., earthquake input) as the reference; (c) deconvolved waves using top story's response time-series as the reference. From the basement to the top, each curve represents the corresponding story.

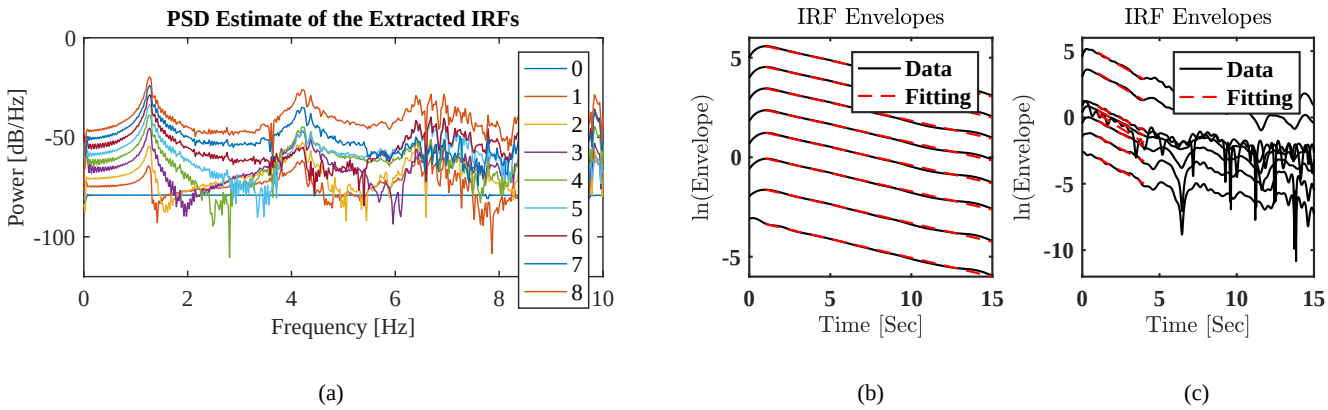

FIGURE 3 (a) PSD estimate of the extracted deconvolved waves of D(0). Each story level is represented by a different color. (b-c) Linear fits for the damping parameter estimations, $\xi_1 = 2.3\%$ in (b) and $\xi_2 = 2.4\%$ in (c) for state D(0). Each curve represents a different floor (from the bottom to the top). Final coefficient values are estimated by taking the average of the slopes of the fitted lines.

wave velocities. Deconvolution with respect to the bottom and the top of the building yields different waveforms, and therefore, the estimated wave velocities are slightly different. Note that for the waves that are extracted through the deconvolution with respect to the top floor's recordings, only the acausal parts are utilized in APM.

It is observed that, given the bolt loosening, both APM and SM can detect the changes/variations in the velocity as an index for damage detection. For both methods, the velocity reduction is more evident for the more severely damaged state, e.g. D(2). In general, as it is demonstrated in Figure 5(c), the SM yields larger velocity variations compared with the APM for both damage states. Hence, in the sense of damage detection, SM might have a better sensitivity.

In the second step of our proposed method, we create a 8-story shear type model accounting for the topology of the structure and the mass of each floor (see Figure 1). We update the proposed FEM against the IRF estimates extracted from the measured data utilizing the described hierarchical Bayesian framework. Herein, we use the extracted IRFs, with respect to the base excitation, of the intact experimental structure. For $\mathbf{M} \in \mathbb{R}^{8\times8}$, mass values of $m_1 = 80$ kg and $m_{2-8} = 75$ kg are used[52]. Stiffness

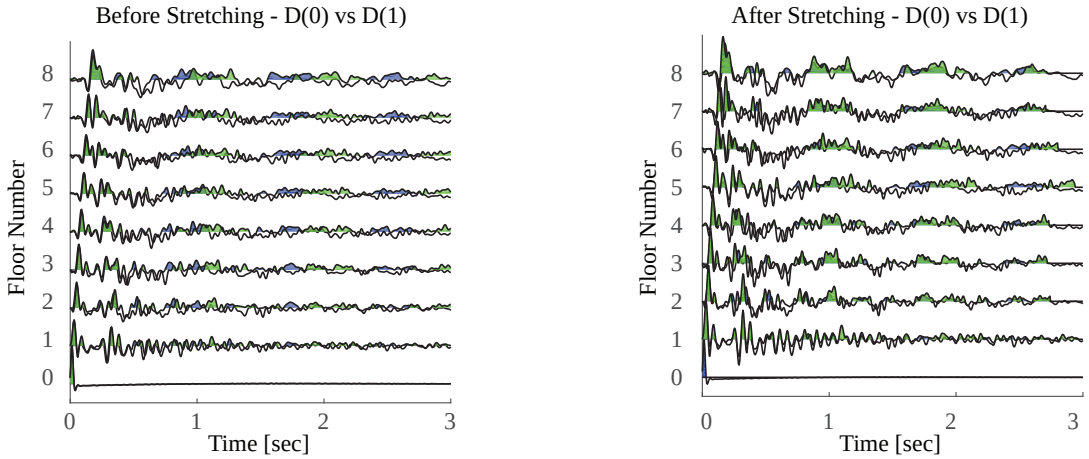

FIGURE 4 Illustration of the SM. Extracted IRFs are shown before and after stretching operation. IRFs that represent the intact state are colored blue. Note that the stretching coefficient is selected so that the correlation between the reference trace and the damaged trace is maximized.

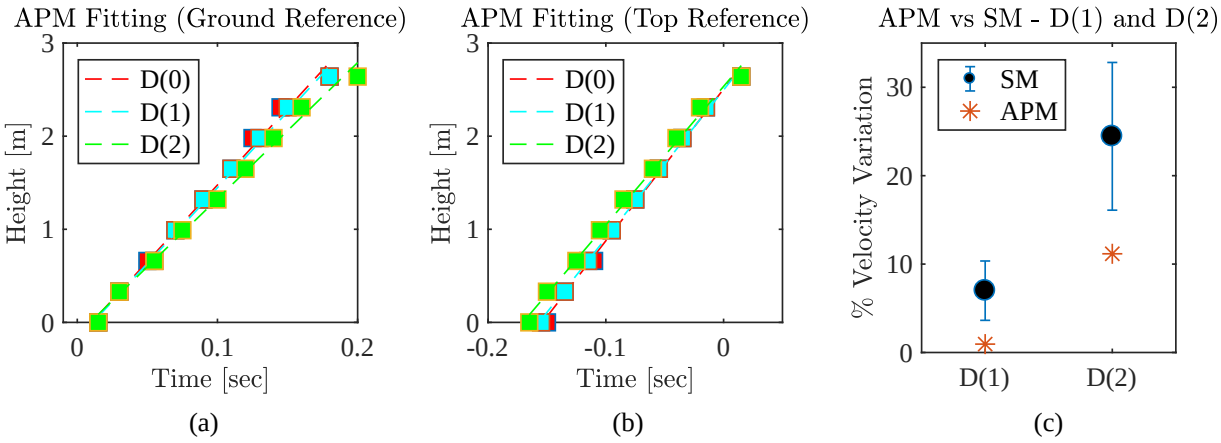

FIGURE 5 (a-b) Shear wave velocity calculation using APM. Note that in (a) the deconvolution functions are calculated using the ground level's acceleration-time series, namely, the earthquake input, as the reference signal, whereas in (b) top-floor's response is used as the reference trace. The slope of the fitted lines corresponds to the estimated intrinsic shear wave velocities. (c) Calculated shear wave velocity variations using the APM and the SM. Error-bars represent the standard deviation of the stretching coefficients that are calculated for each floor for a given damage state.

parameter θ_i's are assumed to have a Gaussian Prior with a mean of 1.25×10^5 N/m with a 30% coefficient of variation (c.o.v) assuming uncorrelated parameters (i.e., $\mathbf{\Sigma}_{\boldsymbol{\theta}} = \sigma_{\theta}^2 \mathbf{I}$). The prior PDF for the prediction error are decided to have hyper-parameters of $\alpha = 10^{-3}$, $\beta = 10^{-6}$. We calculate our likelihood function calculated using Equation 6, for a given model parameter vector $\boldsymbol{\theta}$ and a predefined simulation duration of 7.5 seconds. For sampling, CD is used as a proposal distribution with a constant width parameter, κ, of 0.0032 times the general parameter order of 10^5. The starting point of the chains, $\boldsymbol{\theta}^{(\mathbf{0})}$, is set to be 200 KN/m. The decided chain length, N_{mc}, is 2×10^4 and the burn-in period length, N_{bi}, is 0.5×10^4. We set the lower and upper bounds of the parameters as 0.01×10^5 N/m and 6×10^5 N/m respectively.

The Markov chains that effectively depict the model parameters' marginal posterior PDFs are shown in Figure 6. Note that chains become stationary approximately after 3000 iterations. Histograms that properly describes the updated marginal posterior PDFs are presented in Figure 7. These histograms are constructed using only the retained samples, and the solid red line on each histogram depicts a Gaussian distribution fitted to these samples. The mean values of the updated model parameters are denoted as $\bar{k}_i$ where $i = 1, \ldots .8$. Figure 7 also reports the posterior samples of the prediction error variance, in which the

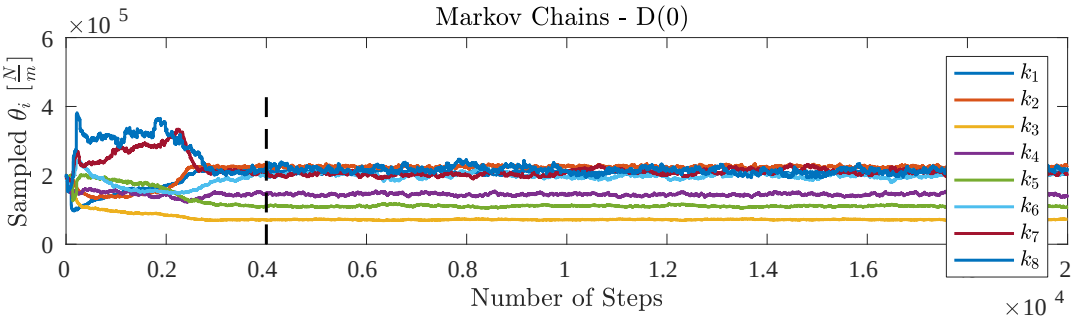

FIGURE 6 Markov chains, that represent the marginal posterior distributions of the stiffness parameters of the intact experimental structure, D(0). Black dashed-line indicates the pre-determined burn-in period, $N_{bi} = 4000$.

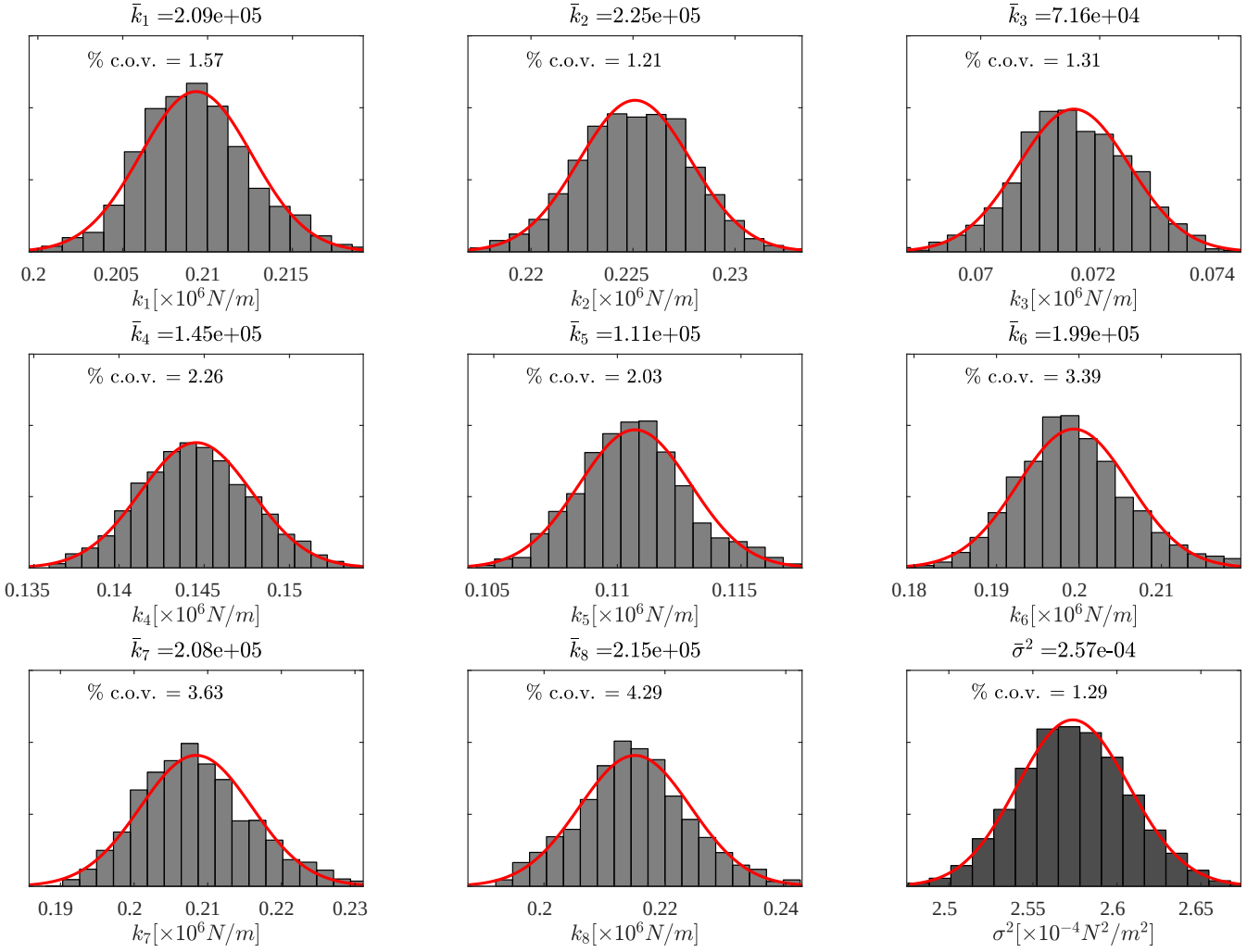

FIGURE 7 Updated posterior PDFs of the model parameters of the intact (i.e., D(0)) experimental structure. Each histogram effectively represents the marginal posterior distribution estimate of the corresponding model parameter, e.g., story stiffness parameters. The red line on each plot depicts the fitted Gaussian distributions for story stiffnesses and the fitted log-normal distribution for the prediction error variance. The mean value of each model parameter is placed on top of each histogram. C.o.v. values of the retained samples are indicated in the figure legends.

TABLE 1 The most probable values (MAP) of the updated model parameters for D(0).

k_i	Identified MAP value [N/m]	c.o.v.(%)	k_i	Identified MAP value [N/m]	c.o.v.(%)
k_1	2.09×10^5	1.57	k_5	1.10×10^5	2.03
k_2	2.25×10^5	1.21	k_6	1.98×10^5	3.39
k_3	0.71×10^5	1.31	k_7	2.07×10^5	3.63
k_4	1.45×10^5	2.26	k_8	2.13×10^5	4.29

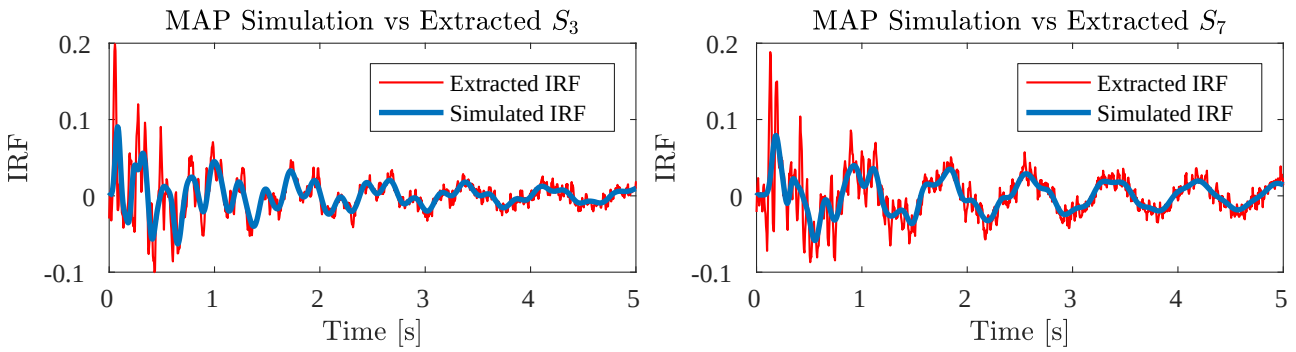

FIGURE 8 Comparison of the extracted vs simulated IRFs/deconvolved waves of D(0). Simulated time-series are produced using the point MAP estimates of the model parameters. Observe that each S_i corresponds to the i^{th} story's IRF.

solid red line denotes the fitted log-normal distribution. It is apparent that the log-normal distribution successfully portrays the drawn prediction error variance samples, which have a small standard deviation. Table 1 outlines the MAP estimates of the model parameters along with the respective c.o.v. values. It can be seen that the MAP estimates range between 71 KN/m and 220 KN/m. Table 1 additionally highlights that c.o.v. values generally increase with the story height. Figure 8 presents a comparison between the extracted and the simulated IRFs (S_3 and S_7) of the intact test structure. Simulations are carried out using the point MAP estimates of the model parameters and the illustrated results are interesting in several ways. First, both figures indicate that updated shear-type model is capable of capturing the later parts of deconvolved waves without any phase and amplitude difference. This would appear to prove the accuracy in the identification of the fundamental mode's damping coefficient (i.e., ξ_1). Second, the observed amplitude discrepancies at early times could indicate the limitations of the selected damping model, i.e., Rayleigh damping, as we only account for the first two mode's attenuation characteristics in constructing the proportional damping matrix. The used damping model seems to overly dampens out the impulse-like interferences of the overtones. One possible solution to alleviate this issue is to use a high-order damping model (e.g., the generalized Cauchy damping). Nevertheless, we can still state that the satisfactory agreement is achieved using the point MAP estimates of the parameters. We cannot rule out the fact that our framework yields probability distributions of the model parameters, therefore before any critical decision, additional analysis should be performed assessing other plausible parameter values.

4.1.1 | Validation of the updated intact model - D(0)

In order to validate our identified intact model, we carry out additional simulations utilizing the fitted Gaussian PDFs. The red lines in Figure 7 depict the utilized PDFs. Herein, we aim to evaluate the learned structural model by comparing it with response measurements of another shake-table experiment of the intact state (i.e., D(0)). This time, we make use of the dataset in which the base excitation was rescaled to match the Kobe earthquake with a peak ground acceleration (PGA) value of 0.09g. Using the same EQ base input for our updated model, we run 1000 finite element simulations in which each story's stiffness parameter is sampled from its fitted marginal posterior within $\pm 3\sigma_{\theta_i}$, where σ_{θ_i} represents the standard deviation of the fitted Gaussian PDF. The comparison results, in terms of the displacement response, for the third story and the seventh story are shown in Figure 9. The predicted displacements, depicted with green lines, are in good agreement with the doubly-integrated acceleration time series, depicted with a blue line, of the experiment. Note that even though every FEM simulation is performed with different

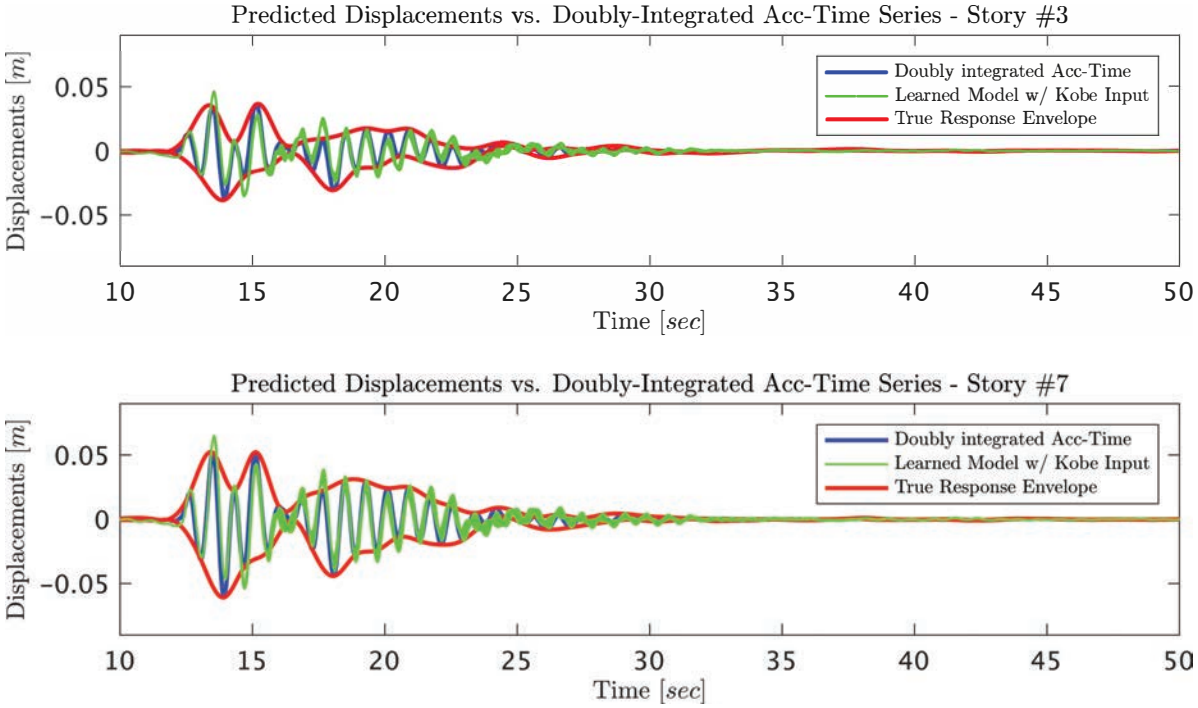

FIGURE 9 Baseline model validation using another EQ input. Observe that the learned model's response prediction agrees well with the doubly integrated acceleration measurements. .

model parameter samples, the displacement response behavior only slightly alters, since the marginal posteriors have small c.o.v. values. This result demonstrates the validity of the initial model class assumption for our identification problem.

4.1.2 | Damage localization and quantification

We herein aim to localize and quantify the damage induced by bolt loosening. In particular, we repeat the previously described identification steps utilizing the earthquake response data of the damaged test structure, specifically, D(1). It is important to note that the damping coefficients are re-estimated using the damaged waveforms, as $\xi_1 = 3.1\%$ and $\xi_2 = 2.2\%$. Preserving the same prior assumptions with the baseline structure (i.e., D(0)), we again learn the posterior parameter distributions of the shear type FEM.

The most remarkable observation is the evident stiffness reduction in k_1 and k_2 as shown in Figure 11. Comparing identified point MAP values from D(0) and D(1) it is observed that the MAP estimates of the first and second story inter-story stiffness parameters reduce 65% and 70% respectively. Considering the nature of the damage via bolt loosening which occurs at the first story for D(1), stiffness reduction in k_1 and k_2 is consistent with the expectations since both the first and the second story are connected to the loosened bolt. In this case, the damage can be quantified based on the shifts of the distributions despite that variation of the distributions of other story stiffness parameters are present. For example, compared with the intact case, point MAP values of k_6, k_7, and k_8 increases 30%, 25% and 12% respectively. However, the observed differences in other model parameters are not particularly surprising given the fact that our framework assumes linearity before and after the damage, yet we cannot rule out the nonlinearities at the bolted interface. This also could be the reason of the observed increase in c.o.v. values. Additionally, inspecting the model parameter's marginal posterior distributions, it is seen that apart from k_1 and k_2, only other updated model parameter that indicates reduction in stiffness, i.e. a false positive error, is k_4. To minimize the discrepancy between the extracted and the modeled impulse-response behavior, the presented framework adjusts the stiffness values of the undamaged story's as well. It is also noted that bolt loosening at the column and slab connections induces non-conventional damages (unlike the column cross-section reduction), leading to additional uncertainties in model updating. Apart from this expected discrepancy, the localization capability of our approach appears to be well substantiated by the % changes of the identified MAP values of the model parameters. Significant stiffness reductions in both k_1 and k_2 indicates the plausible location of the damage.

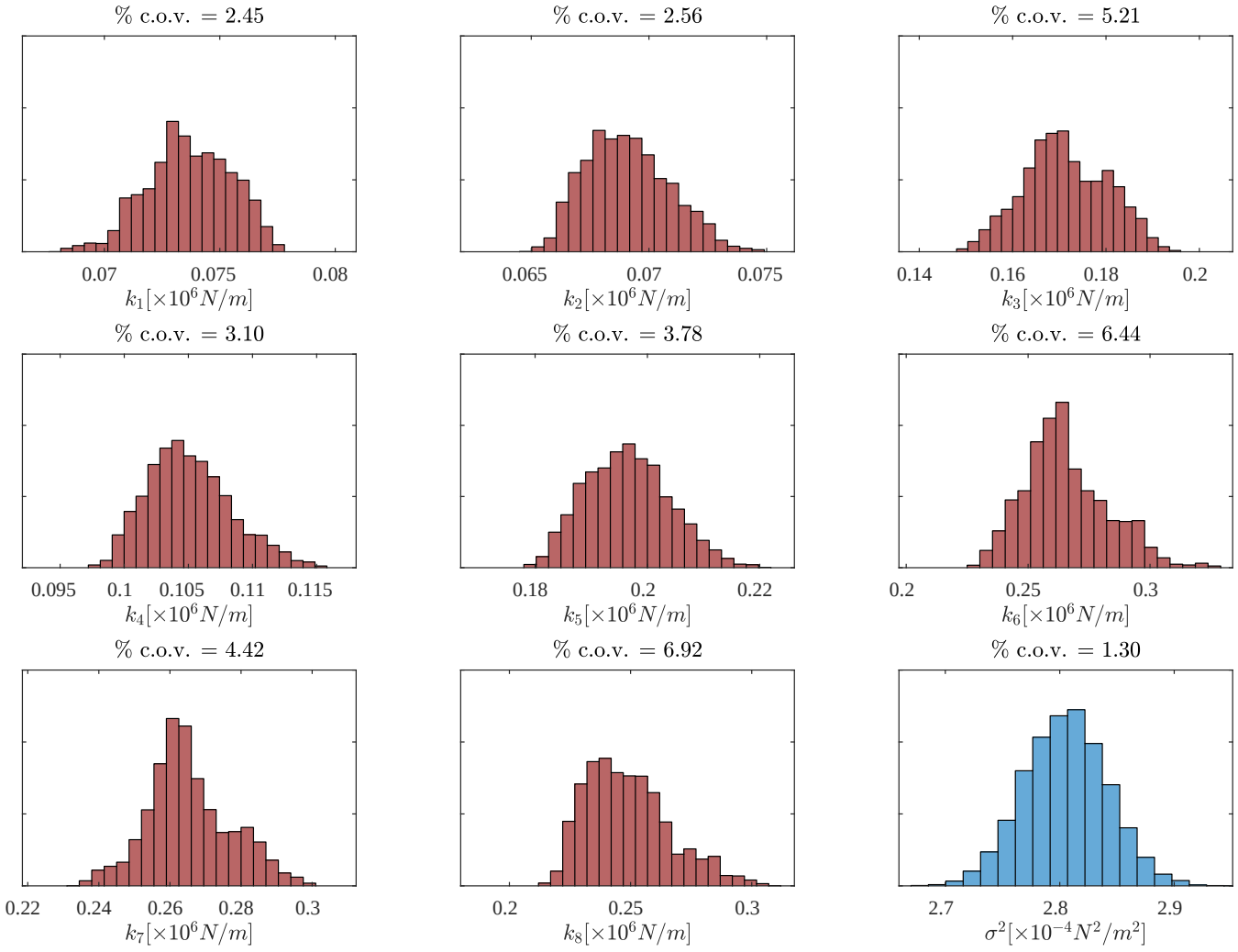

FIGURE 10 Histograms that effectively represent marginal posterior PDFs of the model parameters of the damaged experimental structure, D(1). C.o.v. values are specified on top of each histogram.

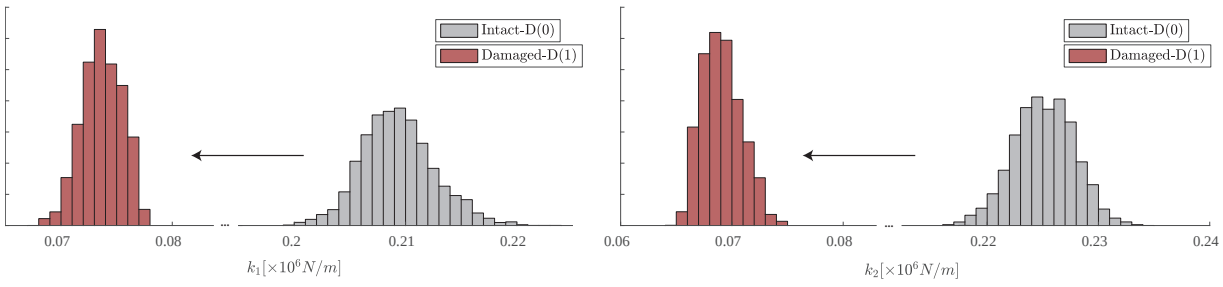

FIGURE 11 Histograms that describe marginal posterior PDFs of (a) first story, (b) second story before and after induced damage, i.e., D(0) and D(1).

4.2 | Experimental Case Study 2: Full-scale 7-story Reinforced Concrete Building Slice

The test structure is a full-scale reinforced concrete (RC) building slice that consists of an RC web wall for lateral resistance in the direction of earthquake loads, a flange wall for transverse resistance, concrete slabs that are supported by four gravity columns,

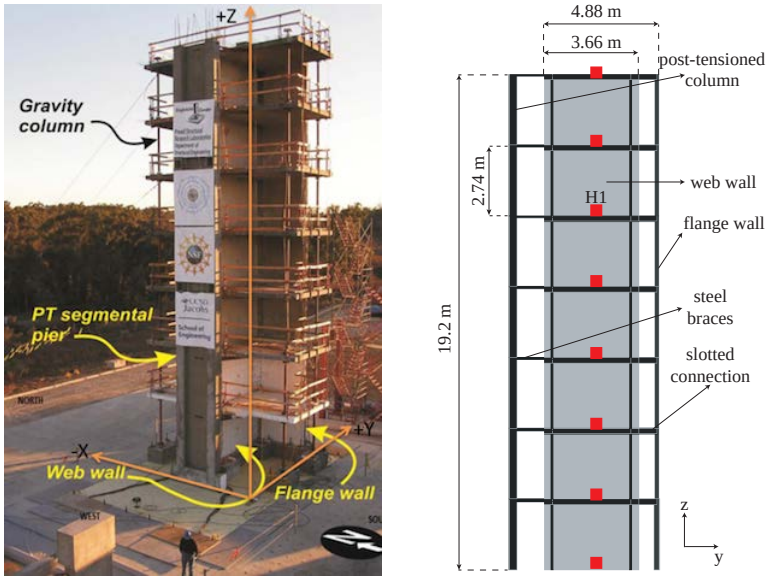

FIGURE 12 Left: 7-storey UCSD-NEES building slice[58]. Right: Elevation view of the structure with the used accelerometer layout. Note that the accelerometers (i.e., 'H1') are illustrated as red squares.

and a precast segmental post-tensioned concrete column to maintain torsional strength[57–59]. More detailed information about the structure and the instrumentation could be found in [60–62]. It is important to note that in this study, we use the recordings from the accelerometers that were placed on the closest slabs to the centroid of the web wall, which were sampled at a rate of 240 Hz. These measurement channels are labeled as 'H-1'. The picture and a sideview of the test structure with the used accelerometer layout[63] are shown in Figure 12.

Shaking experiments were performed between October 2005 and January 2006 using four historical earthquake records of increasing intensity so that progressive structural damage could develop. The corresponding PGA values of these input excitations ranged from 0.15g to 0.91g. At each damage level, meaning that after each earthquake shaking, low amplitude Gaussian and ambient vibration tests were performed. These tests are named S0, S1, S2, S3, and S4 where S0 indicates the undamaged baseline state and Si indicates the damage state after shaking the test structure with the vibration record of i^{th} earthquake. It should be noted that state S3 was divided into S3.1 and S3.2 because before exciting the test structure with the last EQ motion the bracing system between the post-tensioned precast column and the slabs was stiffened[64]. Table 2 specifies the dynamic tests that are used in our study. Low amplitude Gaussian excitations ($0.03g$ and $0.05g$) provide an informative dataset that has been studied by several researchers[64–68].

Figure 14 and Figure 15 show the propagation of waves (e.g., the IRFs at different floor elevations) taking the ground and top floor measurement as the reference, respectively. Note that in Figure 15 IRF_{top} denotes that the deconvolution was performed using the top floor's acceleration-time series as the reference. Figure 14 clearly illustrates that as the imposed damages accumulate on the test structure, propagation characteristics of the shear waves alter. This could be due to concrete cracking and reinforcement yielding. The differences are visually more trackable if the deconvolution is performed using the shake-table's acceleration recordings as the reference signal.

Table 3 reports the wave velocities estimated by the APM utilizing $IRFs$ and IRF_{top}s. The most serious decrease is observed after the last but the most strong earthquake shaking. As presented in Figure 16, the utilized segments of the waves could change/affect the velocity variation estimations by the SM, and therefore the findings need to be interpreted with caution. It is observed that if the initial parts of the waves are used (i.e., $0 \leq t \leq 3$,) then output percent variations from both methods are more comparable. The findings of the SM provide additional support regarding its damage sensitivity compared to the APM. Additionally our analysis reveals that stiffening the slabs and the post-tensioned precast column between S3.1 and S3.2 causes an increase in the estimated velocity values. Taken together, these findings are in line with previous results from the previous case study.

Before deploying our Bayesian model updating scheme to quantify the damage state of the test structure, it is necessary to establish an initial FEM to obtain a reasonable parameter set (i.e., $\mathbf{K}$ and $\mathbf{M}$). Therefore, a primary linear elastic finite element

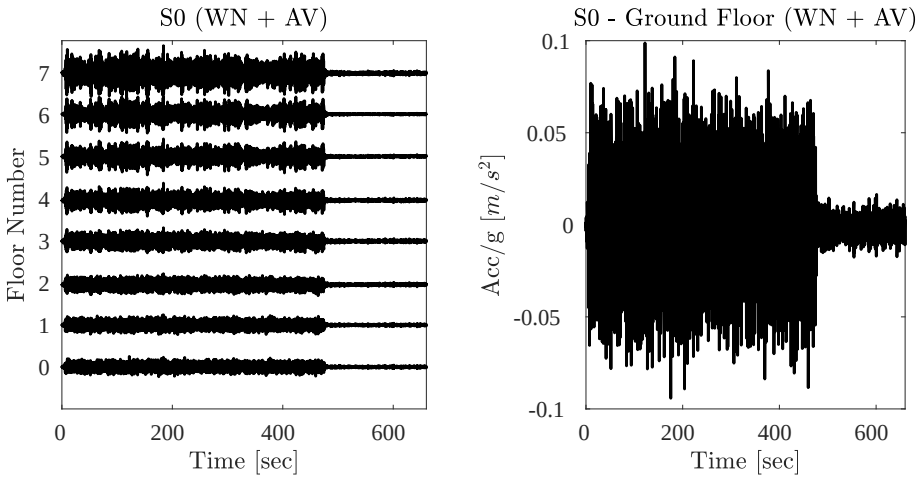

FIGURE 13 Left: Acceleration-time histories of the low-amplitude Gaussian excitation of the intact state, S0. From the basement to the top, each curve represents the acceleration response of the corresponding story. Right: Recordings at ground level.

TABLE 2 Dynamic tests used in this study (Data[64]). WN = white-noise table input; AV = ambient vibration.

Test #	Test Description	Damage State
39	8 min WN(0.03g) + 3 min AV	S0
41	8 min WN(0.03g) + 3 min AV	S1
46	8 min WN(0.03g) + 3 min AV	S2
49	8 min WN(0.03g) + 3 min AV	S3.1
61	8 min WN(0.03g) + 3 min AV	S3.2
64	8 min WN(0.03g) + 3 min AV	S4

TABLE 3 UCSD-NEES structure: Shear wave velocity estimates and percent changes using the APM

	(Ground Ref.)		(Top Floor Ref.)	
State	Estimated Velocity [m/s]	% Change	Estimated Velocity [m/s]	% Change
$S0$	401.7	–	377.3	–
$S1$	388.7	-3.2	362.7	-3.9
$S2$	364.5	-9.2	346.3	-8.2
$S3.1$	333.1	-17.1	331.1	-12.2
$S3.2$	341.8	-14.9	322.2	-14.6
$S4$	204.7	-49.0	262.9	-30.3

model is developed using commercially available structural analysis software ETABS (Computers and Structures, Inc.) based on the available structural drawings. The web wall, the flange wall, and the post-tensioned column are modeled as concrete wall sections (using thin shell elements) with material properties that were extracted from concrete cylinder tests that were performed for each constructed story of the building slice (reported in [68]). The post-tensioned column is approximated as a wall section with an effective width to account for the total section area and the mass. This assumption decreases the torsional stability of our FEM. Slabs are modeled using thin shell elements and to account for the slotted connection for the floor sections that are in between the web wall and the flange wall, out of plane moments are released. [58] reported that with this geometry slabs behave

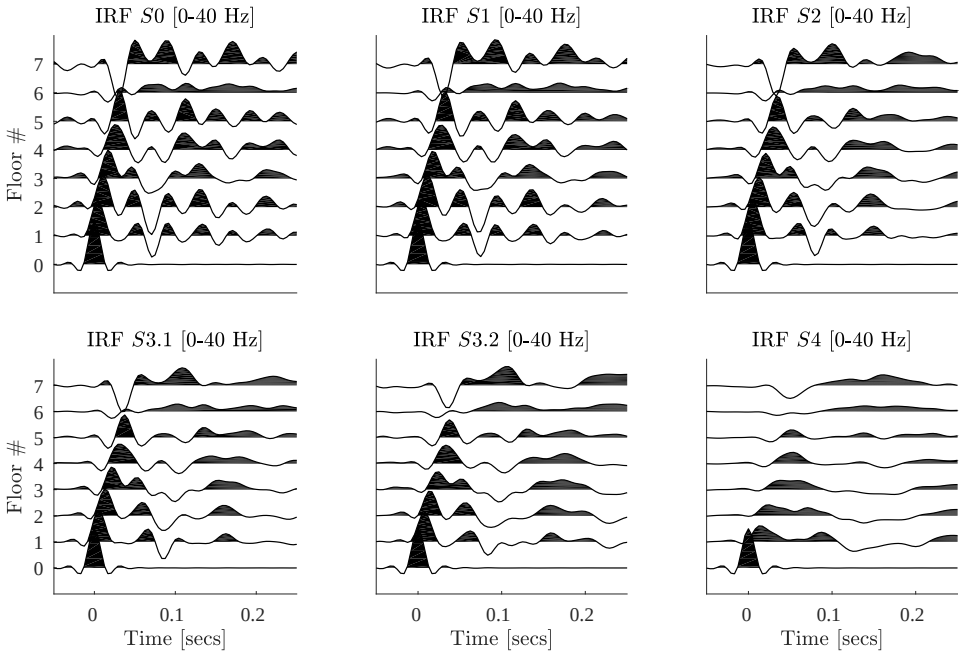

FIGURE 14 Extracted IRFs from low-amplitude Gaussian shakings of different damage states. Ground floor-acceleration recordings were used as the reference signal. Each curve on each plot represents a different floor.

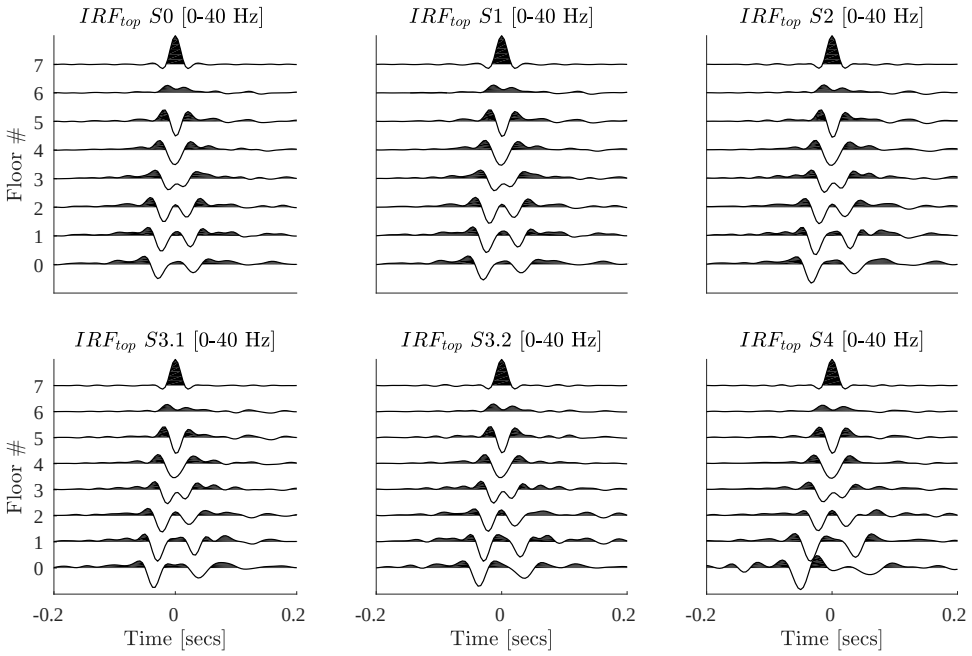

FIGURE 15 Extracted IRFs from low-amplitude Gaussian shakings of different damage states. IRF_{top} denotes that the deconvolutions were performed using the top floor's acceleration-time series as the reference. Each curve on each plot represents a different story.

like a *near-pinned link* that transfers the in-plane forces and moments while reducing the out-of-plane ones. Gravity columns within each story and braces between the post-tensioned pre-cast column and the building slice floors are modeled as truss elements with their corresponding section properties from structural drawings. Note that the structural details of the foundation level are not considered. The natural frequencies with their corresponding mode shapes of the FEM are computed through modal

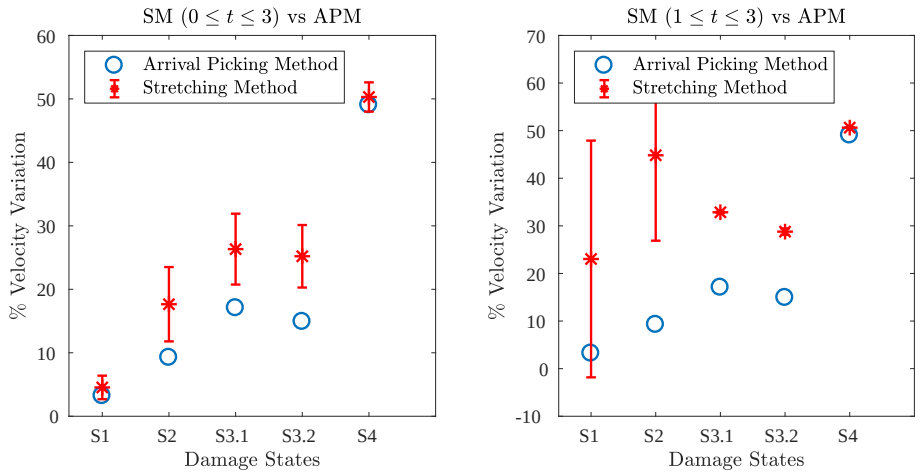

FIGURE 16 Shear wave velocity variations using both the APM and SM for each damage state, i.e., S0, S1, S2, S3.1, S3.2, S4. The utilized time intervals in the SM are indicated on the titles of each plot. Error-bars represent the standard deviation of the stretching coefficients that are calculated for each story for a given damage state.

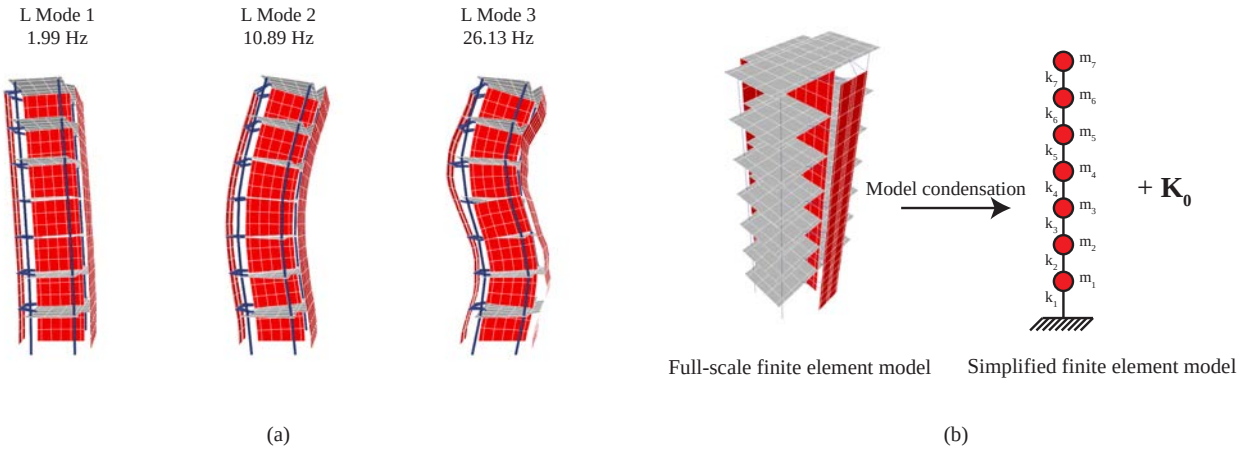

FIGURE 17 (a) Modal analysis results of the ETABS model. (b) Illustration of the model condensation scheme. Note that m_i and k_i represent lumped foor mass and lateral stiffness of each story i.

analysis. The acquired analytical results are within the acceptable agreement with the modal information of the accelerometer data that is derived from the damage state S0, i.e., Test 39, by state-of-the-art linear system identification methods (see [64] for details). Figure 17(a) illustrates the first three longitudinal modes, i.e., 1.99 Hz, 10.89 Hz of the model ETABS structure.

Assuming in-plane rigid diaphragms, the earthquake response of the full structure can be characterized by computing the drifts at the center of mass locations of each diaphram. Therefore, we condense the full-scale finite element model into a discretized shear-type model, as it illustrated in Figure 17 (b). This simplification essentially reduces the number of parameters so that Bayesian learning procedures become computationally affordable. Primary lateral stiffness matrix, i.e., $\mathbf{K_0}$, and the diagonal lumped mass matrix, i.e., $\mathbf{M}$, are constructed using the procedure described in [69] and [39]. The procedure is based on assembling the lateral flexibility matrix by applying unit loads to each story level while tracing the story drifts. $\mathbf{K_0}$ is then computed by taking the inverse of the acquired flexibility matrix. Having a primary stiffness matrix enables us to define a substructure that could be parametrized and updated. Full stiffness matrix, $\mathbf{K}$, can be described as [39]

$$\mathbf{K} = \mathbf{K_0} + \sum_{i}^{N_\theta} \theta_i \mathbf{K_i} \tag{11}$$

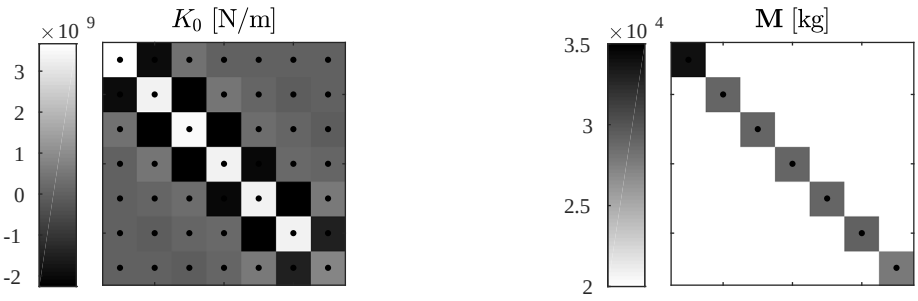

FIGURE 18 Illustration of the condensed primary stiffness matrix, $\mathbf{K_0}$, and mass matrix $\mathbf{M}$. These matrices are constructed using the full-scale ETABS model.

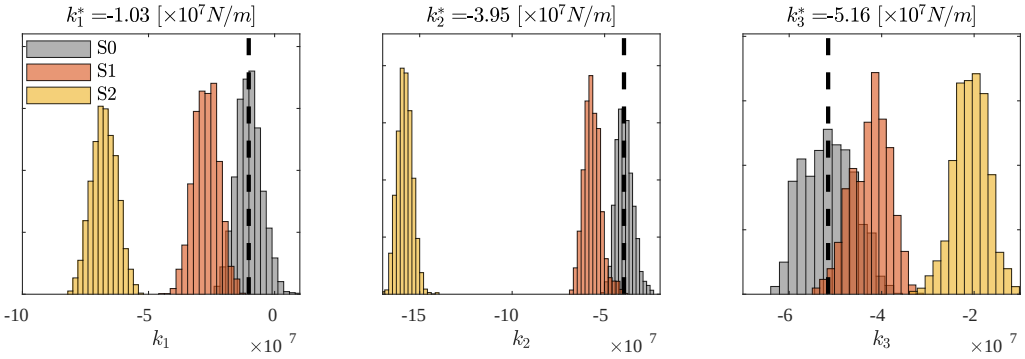

FIGURE 19 Posterior samples of k_1, k_2 and k_3 from damage states S0, S1, and S2. Black dashed lines denote the median values, k_i^*, of the posterior samples for state S0.

where, $\mathbf{K_i}$ denotes the stiffness of the i^{th} sub-structure, and N_θ corresponds to the total number parameters. Our substructure is a linear shear-type model that goes into the mathematical class $\mathcal{M}$, and its dynamical behavior follows Equation (**??**). Figure 18 illustrates the obtained primary stiffness ($\mathbf{K_0}$) and mass ($\mathbf{M}$) matrices. The value of each matrix element is color-coded using the respective colorbars. It can be seen that the primary stiffness matrix is not exactly band-limited yet the concentration is around the main diagonal with a general order of 10^9 N/m. Similarly a diagonal mass matrix is assembled using the story mass values of the ETABS model as $m_1 = 3.40\times10^4$, $m_{2,3,4,5} = 2,89\times10^4$, $m_6 = 2.91\times10^4$, and $m_7 = 2.78\times10^4$ kg. These values correlate satisfactorily well with the previously reported story weights of the test structure in [58].

By applying the presented Bayesian updating scheme, we determine the posterior distributions of the model parameters using the extracted IRFs from damage states S0 (Test #39), S1 (Test #41), and S2 (Test #46). For each damage state the damping coefficients, $\xi_{1,2}$, are re-determined and used in constructing our condensed model's damping matrix $\mathbf{C}$. As shown in the bottom part of Table 4, our estimated attenuation coefficients lie within an acceptable range interval of the modal damping ratios that was previously reported in [64]. This similarity is expected as the structural response can be equivalently described by modal superposition. It is observed that the damage accumulation increases the exponential decay rate of the IRF amplitudes. Initial assumptions for FEM updating procedure are as follows: Each model parameter is assumed to have a Gaussian prior PDF with a mean of zero and a standard deviation of 5×10^6 N/m. Similarly to the previous case studies, a Cauchy distribution (CD) is used as the proposal PDF. Its width parameter κ is set to the 0.05% of the general parameter order. Other hyper-parameters are selected the same as the previous case study. At each iteration the full stiffness matrix is computed using Equation 11. Note that the resultant IRFs from the response data are bandpass filtered ([0.5, 25] Hz) and then used in the calculation of the likelihood (Equation 6). We create Markov chains with a length of 2×10^4 and discard the first 1×10^4 samples. It should be noted that with the assumptions mentioned earlier the observed acceptance rate of our MCMC sampling is around 50%.

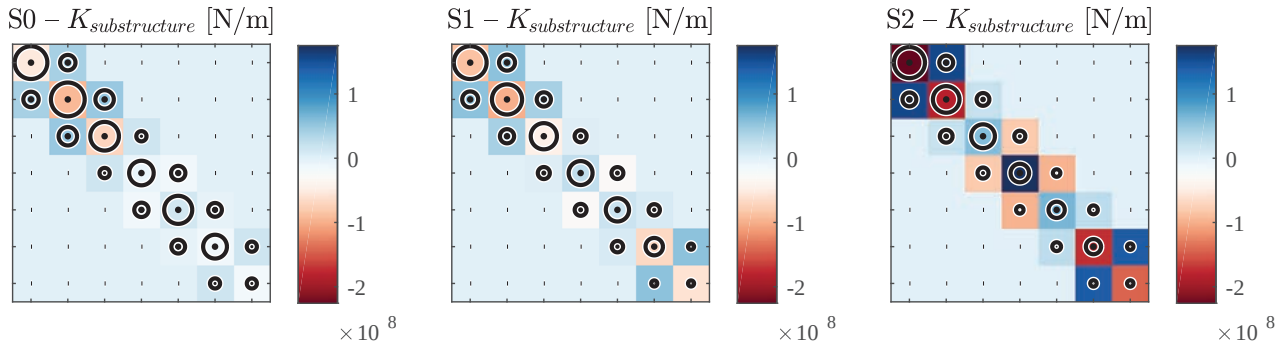

FIGURE 20 From left to right: Substructure's updated stiffness matrices that respectively corresponds to damage states S0, S1, and S2. Coloring is performed according to the median values of the model parameters' marginal posterior samples. Normalized standard deviations are indicated as black circles.

TABLE 4 Identified median estimates of the model parameters and identified damping coefficients from damage states S0, S1, and S2

k_i	Identified median value [$\times 10^7$N/m] S0	Identified median value [$\times 10^7$N/m] S1	Identified median value [$\times 10^7$N/m] S2
k_1	−1.02	−2.71	−6.76
k_2	−3.95	−5.70	−15.82
k_3	−5.16	−4.20	−2.06
k_4	−1.71	−0.29	7.93
k_5	1.20	2.92	9.59
k_6	0.20	−0.93	−2.99
k_7	−1.57	−5.73	−14.15
ξ_1	3.69%	3.89%	5.13%
ξ_2	4.88%	6.30%	7.02%

Figure 19 shows the histograms that effectively portray the posterior PDFs of substructure's first there stories' lateral stiffness parameters, i.e., k_1, k_2, and k_3. For the first and the second stories, clear shifts in the distributions can be observed. This is in a good agreement with our expectations as the lower stories of the test structure are subjected to relatively higher shear forces and bending moments during the EQ loading. However, for k_3 the direction of the shift corresponds to an increase in the inter-story lateral stiffness of the third story our shear-type substructure. As illustrated in Figure 20, similar trend can be recognized for other model parameters by inspecting the color-coded band-limited stiffness matrices that are assembled using the median values of the posterior chains. Note that the normalized standard deviations of the respective model parameters are indicated with black circles with changing radiuses. It can be seen that the width of the posterior PDFs generally decrease with the increasing story height. This effect could be due the primary stiffness matrix $\mathbf{K_0}$. Another interesting observation which could also be attributed to the complex coupling between $\mathbf{K_0}$ and $\mathbf{K}_{substructure}$ is that the direction of the shift of the marginal posterior PDFs does not change as the damage accumulates. For example, as detailed in Table 4, while k_1 and k_2 decreases as a function of damage, k_4 and k_5 increases. Additionally, estimated median values for the prediction error variances are $\sigma^2 = 9.32 \times 10^{-5}$ for S0, $\sigma^2 = 7.91 \times 10^{-5}$ for S1, and $\sigma^2 = 7.42 \times 10^{-5}$ for S2. Figure 21 shows, from top to bottom, the simulated IRFs in comparison with the IRFs obtained from low amplitude Gaussian test for damage states S0, S1, and S2. Simulations are carried out using the median estimates of the inter-story stiffness parameters. Clear agreement confirms the capability of our shear-type model and the used condensation scheme.

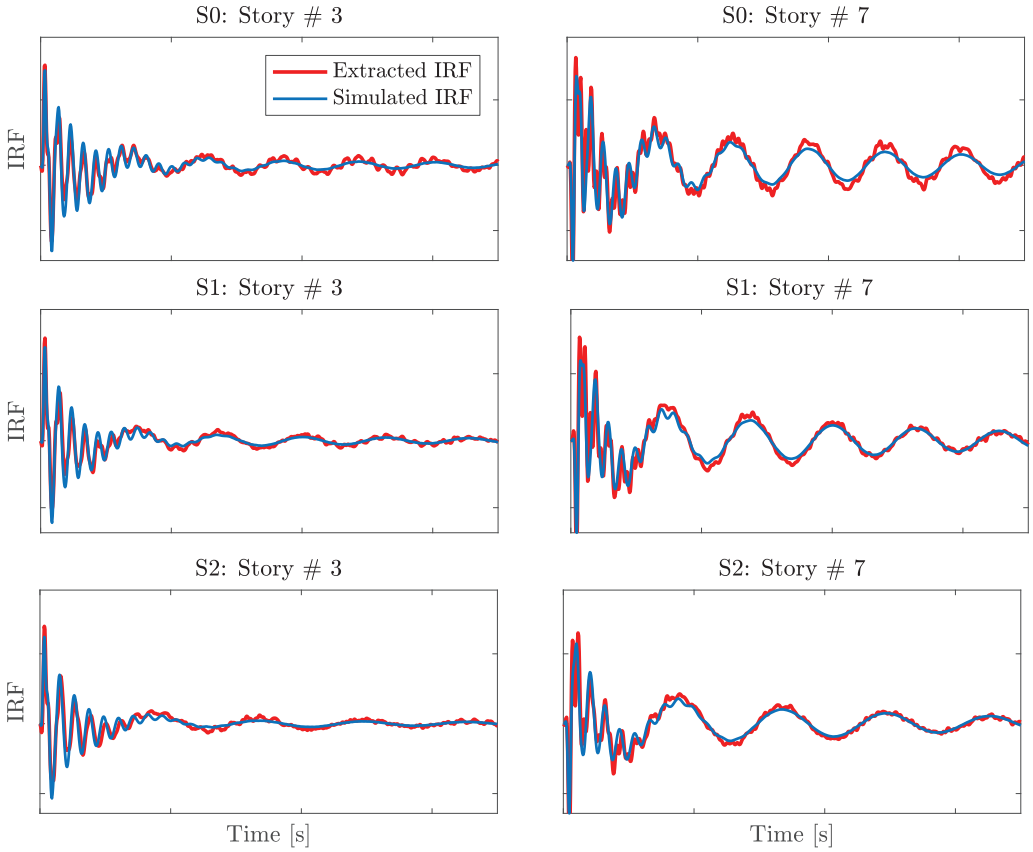

FIGURE 21 Comparison of the extracted vs. reconstructed IRFs of the test structure. From top to bottom each figure depicts the comparison of 3^{rd} and 7^{th} stories' impulse response behavior for damage states S0, S1, and S2 respectively. Simulated time-series are created using the point median estimates of the model parameters.

5 | CONCLUSIONS AND DISCUSSION

5.1 | Discussion

Results indicate that the presented framework is promising for monitoring structural systems. It allows for non-invasive determination of structural parameters. Studying the extracted IRFs in the time-domain provides a qualitative information about the state of the damage in the structure. The location of the reference signal (i.e., ground story or top story) for the deconvolution operation does not affect the content of the information, however, both operations are advised as one of them could be easier to analyze, especially if the damage state is severe. Variations in the shear wave velocities are observed to be correlated with severity of the accumulated damage. Our results indicate that the SM could be more favorable for minor damage states. The capability of the method, however, depends on the selected time interval for the stretching operation. In addition, through comparison of the deconvolved waveforms that are extracted from different ground inputs with different strengths (e.g., different earthquakes), potential nonlinearities can be observed and utilized as a damage indicator.

Time-series of the extracted IRFs can be coupled with hierarchical Bayesian identification schemes. Using the updated simplified models (i.e., marginal posterior PDFs) damage quantification is possible (e.g., shifts in the parameter histograms). The observed minor discrepancies in the early times of the IRFs could imply the limitations of the used damping model as the updated model partially fails to reproduce the impulse-like/high amplitude response behavior of the experimental structure. Comparing the representative posterior histograms of different damage states, observed shifts in the distributions that correspond to the stiffness reductions are generally in good agreement with the expected/known damaged regions of the structure. However, other marginal posterior PDFs are also affected. This could be due to the potential nonlinearities, modeling assumptions, i.e., our shear-type models may be too simple to fully capture the dynamics of the experimental structures, and used model condensation scheme.

It should be noted that, as the complexity of the model increases, Bayesian model updating becomes more challenging. To be able to obtain the correct parameter set (given an identifiable model), mechanically meaningful parameter ranges, and a reasonable step size for MCMC should be chosen. A key realization is that modeling errors as well as poor identification of damping values could yield inconclusive identification results, e.g., non-converging Markov chains. In particular, full-scale structures could require condensed FEMs for the successful parameter identification and damage quantification. A further research in finite element model reduction as well as damping modeling and identification could benefit the presented procedure.

5.2 | Conclusion

We present a computational approach for structural identification and damage detection using the concepts of seismic interferometry and the Bayesian inference. To assess the damage (location and severity), Bayesian inference with MCMC sampling is utilized through quantifying parameter uncertainties of an FEM using the extracted IRFs. We initially analyze the shake-table experiment dataset that contains various damage scenarios, which are induced via loosening the bolts. We show that the variations in the shear wave velocity (using both APM and SM) can be used for quick damage detection, and that the velocity reduction is more evident for the more severely damaged states. We then, using the extracted IRFs of the shaking experiment, update our shear-type FEM. Using the MAP point estimates of the model parameters, which are determined from the posterior samples, we confirm that the extracted IRFs of the experimental structure and the simulated impulse response behavior of the FEM compare well with each other. Additionally, we validate the updated baseline FEM, by comparing the simulated displacement-time series with the doubly integrated acceleration response measurements for another EQ base input. We demonstrate that the induced damage, i.e., bolt-loosening on the first floor, affects the posterior distributions of the model parameters quite noticeably. It is observed that the potential damaged region of the test structure can be identified by inspecting the statistical changes of the posterior samples of the updated model parameters.

To test our procedure on a full-scale structure, we study the propagating seismic waves that are derived from the RC building slice shake-table experiment. Throughout the experimental program, the test structure was deliberately damaged by increasing the intensity of the induced shaking. Examining the collected structural acceleration response data-sets of low-amplitude Gaussian (e.g., $0.03g$) and ambient vibration tests, it is observed that the for each damage state the propagation characteristics of the seismic shear waves changes. For highly-damaged states (e.g., S4) these differences could be visually noticed from the IRF vs. the structural elevation plots. We further our analysis of the deconvolved waves using the APM and SM, and compute the shear wave velocity variations as a function of the damage state. Since our primary aim is to link the obtained IRFs to the model characteristics of the building that could inform us about the current state of the structure, we established a full scale FEM of the test structure from its structural drawings. Subsequently, a model condensation procedure is implemented to deploy our computationally intensive parameter identification framework. Results indicate that the simulated IRFs of our condensed model agrees quite well with the extracted IRFs. In parallel with our initial case study, by comparing the deviations of the model posteriors, imposed damage can be quantified. It should be noted that updated structural models can be used to predict structure's performance in the presence of a possible earthquake and further coupled with seismic fragility assessment framework.

6 | ACKNOWLEDGMENTS

The authors acknowledge the support provided by Royal Dutch Shell through the MIT Energy Initiative. We would like to thank Professor Babak Moaveni for providing the formatted dataset of the UCSD-NEES structure. We greatly appreciate the insightful comments of Dr. Justin Chen, Dr. James Long, and Dr. Reza Mohammadi Ghazi on our manuscript. We also acknowledge the National Center for Research on Earthquake Engineering (Taiwan) for sharing the shaking table test data used in this paper to validate the proposed algorithm.

References

1. Salawu OS. Detection of structural damage through changes in frequency: a review. *Engineering structures.* 1997;19(9):718–723.

2. Toksoy T, Aktan AE. Bridge-condition assessment by modal flexibility. *Experimental Mechanics.* 1994;34(3):271–278.

3. Tseng Kevin K, Wang Liangsheng. Impedance-based method for nondestructive damage identification. *Journal of engineering mechanics.* 2005;131(1):58–64.

4. West Walter M. Illustration of the use of modal assurance criterion to detect structural changes in an orbiter test specimen. 1986;.

5. Stubbs N, Kim JT, Topole K. An efficient and robust algorithm for damage localization in offshore platforms. In: :543–546; 1992.

6. Montalvão Diogo, Ribeiro AMR, Duarte-Silva J. A method for the localization of damage in a CFRP plate using damping. *Mechanical systems and signal processing.* 2009;23(6):1846–1854.

7. Farrar Charles R, Worden Keith. An introduction to structural health monitoring. *Philosophical Transactions of the Royal Society of London A: Mathematical, Physical and Engineering Sciences.* 2007;365(1851):303–315.

8. Worden Keith, Farrar Charles R, Manson Graeme, Park Gyuhae. The fundamental axioms of structural health monitoring. In: :1639–1664The Royal Society; 2007.

9. Farrar Charles R, Worden Keith, Todd Michael D, et al. *Nonlinear system identification for damage detection.* : Los Alamos National Laboratory (LANL), Los Alamos, NM; 2007.

10. Carden E Peter, Fanning Paul. Vibration based condition monitoring: a review. *Structural health monitoring.* 2004;3(4):355–377.

11. Doebling Scott W, Farrar Charles R, Prime Michael B, others . A summary review of vibration-based damage identification methods. *Shock and vibration digest.* 1998;30(2):91–105.

12. Fan Wei, Qiao Pizhong. Vibration-based damage identification methods: a review and comparative study. *Structural Health Monitoring.* 2011;10(1):83–111.

13. Rytter Anders. Vibrational based inspection of civil engineering structures. PhD thesisDept. of Building Technology and Structural Engineering, Aalborg University1993.

14. Şafak Erdal. Wave-propagation formulation of seismic response of multistory buildings. *Journal of Structural Engineering.* 1999;125(4):426–437.

15. Todorovska Maria I. Seismic interferometry of a soil-structure interaction model with coupled horizontal and rocking response. *Bulletin of the Seismological Society of America.* 2009;99(2A):611–625.

16. Kanai Kiyoshi, Yoshizawa Shizuyo. Some New Problems of Seismic Vibrations of a Structure. Part 1.. 1963;.

17. Iwan WD. Drift spectrum: measure of demand for earthquake ground motions. *Journal of structural engineering.* 1997;123(4):397–404.

18. Todorovska Maria I, Trifunac Mihailo D. Earthquake damage detection in the Imperial County Services Building III: analysis of wave travel times via impulse response functions. *Soil Dynamics and Earthquake Engineering.* 2008;28(5):387–404.

19. Nakata Nori, Snieder Roel, Kuroda Seiichiro, Ito Shunichiro, Aizawa Takao, Kunimi Takashi. Monitoring a building using deconvolution interferometry. I: Earthquake-data analysis. *Bulletin of the Seismological Society of America.* 2013;103(3):1662–1678.

20. Nakata Nori, Snieder Roel. Monitoring a building using deconvolution interferometry. II: Ambient-vibration analysis. *Bulletin of the Seismological Society of America.* 2014;104(1):204–213.

21. Rahmani Mohammadtaghi, Ebrahimian Mahdi, Todorovska Maria I. Time-wave velocity analysis for early earthquake damage detection in buildings: Application to a damaged full-scale RC building. *Earthquake Engineering & Structural Dynamics.* 2015;44(4):619–636.

22. Simoen Ellen, De Roeck Guido, Lombaert Geert. Dealing with uncertainty in model updating for damage assessment: A review. *Mechanical Systems and Signal Processing.* 2015;56:123–149.

23. Mottershead JE, Friswell MI. Model updating in structural dynamics: a survey. *Journal of sound and vibration.* 1993;167(2):347–375.

24. Beck James L, Katafygiotis Lambros S. Updating models and their uncertainties. I: Bayesian statistical framework. *Journal of Engineering Mechanics.* 1998;124(4):455–461.

25. Beck James L, Au Siu-Kui. Bayesian updating of structural models and reliability using Markov chain Monte Carlo simulation. *Journal of engineering mechanics.* 2002;128(4):380–391.

26. Beck James L, Au Siu-Kui, Vanik Michael W. Monitoring structural health using a probabilistic measure. *Computer-Aided Civil and Infrastructure Engineering.* 2001;16(1):1–11.

27. Astroza Rodrigo, Ebrahimian Hamed, Conte Joel P.. Material Parameter Identification in Distributed Plasticity FE Models of Frame-Type Structures Using Nonlinear Stochastic Filtering. *Journal of Engineering Mechanics.* 2015;141(5):04014149.

28. Behmanesh Iman, Moaveni Babak, Lombaert Geert, Papadimitriou Costas. Hierarchical Bayesian model updating for structural identification. *Mechanical Systems and Signal Processing.* 2015;64-65:360 - 376.

29. Erazo Kalil, Hernandez Eric M.. Bayesian Model–Data Fusion for Mechanistic Postearthquake Damage Assessment of Building Structures. *Journal of Engineering Mechanics.* 2016;142(9):04016062.

30. Erazo Kalil, Nagarajaiah Satish. An offline approach for output-only Bayesian identification of stochastic nonlinear systems using unscented Kalman filtering. *Journal of Sound and Vibration.* 2017;397:222 - 240.

31. Erazo Kalil, Nagarajaiah Satish. Bayesian structural identification of a hysteretic negative stiffness earthquake protection system using unscented Kalman filtering. *Structural Control and Health Monitoring.* 2018;25(9):e2203.

32. Azam Saeed Eftekhar, Mariani Stefano. Online damage detection in structural systems via dynamic inverse analysis: A recursive Bayesian approach. *Engineering Structures.* 2018;159:28 - 45.

33. Astroza Rodrigo, Ebrahimian Hamed, Li Yong, Conte Joel P.. Bayesian nonlinear structural FE model and seismic input identification for damage assessment of civil structures. *Mechanical Systems and Signal Processing.* 2017;93:661 - 687.

34. Astroza Rodrigo, Alessandri AndrÃĺs, Conte Joel P.. A dual adaptive filtering approach for nonlinear finite element model updating accounting for modeling uncertainty. *Mechanical Systems and Signal Processing.* 2019;115:782 - 800.

35. Ghahramani Zoubin. Probabilistic machine learning and artificial intelligence. *Nature.* 2015;521(7553):452.

36. Snieder Roel, Şafak Erdal. Extracting the building response using seismic interferometry: Theory and application to the Millikan Library in Pasadena, California. *Bulletin of the Seismological Society of America.* 2006;96(2):586–598.

37. Prieto German A, Lawrence Jesse F, Chung Angela I, Kohler Monica D. Impulse response of civil structures from ambient noise analysis. *Bulletin of the Seismological Society of America.* 2010;100(5A):2322–2328.

38. Kohler Monica D, Heaton Thomas H, Bradford Samuel C. Propagating waves in the steel, moment-frame factor building recorded during earthquakes. *Bulletin of the Seismological Society of America.* 2007;97(4):1334–1345.

39. Sun Hao, Mordret Aurélien, Prieto Germán A, Toksöz M Nafi, Büyüköztürk Oral. Bayesian characterization of buildings using seismic interferometry on ambient vibrations. *Mechanical Systems and Signal Processing.* 2017;85:468–486.

40. Snieder Roel, Sheiman Jon, Calvert Rodney. Equivalence of the virtual-source method and wave-field deconvolution in seismic interferometry. *Physical Review E.* 2006;73(6):066620.

41. Snieder Roel. The theory of coda wave interferometry. *Pure and Applied geophysics.* 2006;163(2-3):455–473.

42. Mordret Aurelien, Sun Hao, Prieto German A., Toksoz M. Nafi, Buyukozturk Oral. Continuous Monitoring of High?Rise Buildings Using Seismic Interferometry. *Bulletin of the Seismological Society of America.* 2017;107(6):2759-2773.

43. Tsogka Chrysoula, Daskalakis Emmanouil, Comanducci Gabriele, Ubertini Filippo. The Stretching Method for Vibration-Based Structural Health Monitoring of Civil Structures. *Computer-Aided Civil and Infrastructure Engineering.* 2017;32(4):288-303.

44. Adhikari Sondipon. Damping models for structural vibration. PhD thesisUniversity of Cambridge2001.

45. Knopoff L, Aki K, Archambeau CB, Ben-Menahem A, Hudson JA. Attenuation of dispersed waves. *Journal of Geophysical Research.* 1964;69(8):1655–1657.

46. Aki Keiiti, Richards Paul G. Quantative seismology: Theory and methods. *New York.* 1980;:801.

47. Caughey TK. Classical normal modes in damped linear dynamic systems. *Journal of Applied Mechanics.* 1960;27(2):269–271.

48. Chopra Anil K. *Dynamics of structures: theory and applications to earthquake engineering*. Prentice-Hall; 2001.

49. Beck James L. Bayesian system identification based on probability logic. *Structural Control and Health Monitoring.* 2010;17(7):825–847.

50. Yuen Ka-Veng, Kuok Sin-Chi. Bayesian methods for updating dynamic models. *Applied Mechanics Reviews.* 2011;64(1):010802.

51. Sun Hao, Betti Raimondo. A hybrid optimization algorithm with Bayesian inference for probabilistic model updating. *Computer-Aided Civil and Infrastructure Engineering.* 2015;30(8):602–619.

52. Sun Hao, Büyüköztürk Oral. Probabilistic updating of building models using incomplete modal data. *Mechanical Systems and Signal Processing.* 2016;75:27–40.

53. Au Siu-Kui. Fast Bayesian ambient modal identification in the frequency domain, Part II: Posterior uncertainty. *Mechanical Systems and Signal Processing.* 2012;26:76–90.

54. Geman Stuart, Geman Donald. Stochastic relaxation, Gibbs distributions, and the Bayesian restoration of images. *IEEE Transactions on pattern analysis and machine intelligence.* 1984;(6):721–741.

55. Murray Iain. *Advances in Markov chain Monte Carlo methods*. University of London, University College London (United Kingdom); 2007.

56. Nichols JM, Link WA, Murphy KD, Olson CC. A Bayesian approach to identifying structural nonlinearity using free-decay response: application to damage detection in composites. *Journal of Sound and Vibration.* 2010;329(15):2995–3007.

57. Martinelli Paolo, Filippou Filip C.. Simulation of the shaking table test of a seven-story shear wall building. *Earthquake Engineering & Structural Dynamics.* 2009;38(5):587-607.

58. Panagiotou Marios, Restrepo José I. Displacement-based method of analysis for regular reinforced-concrete wall buildings: Application to a full-scale 7-story building slice tested at UC–San Diego. *Journal of Structural Engineering.* 2010;137(6):677–690.

59. Panagiotou Marios, Restrepo José I, Conte Joel P. Shake-table test of a full-scale 7-story building slice. Phase I: Rectangular wall. *Journal of Structural Engineering.* 2010;137(6):691–704.

60. Panagiotou M, Restrepo JI, Conte JP. *Shake Table Test of a 7-story Full Scale Reinforced Concrete Structural Wall Building Slice, Phase I: Rectangular Section.* : Report No. SSRP-07/07, Department of Structural Engineering, University of California, San Diego, CA; 2007.

61. Panagiotou M, Restrepo JI, Conte JP. Shake table test of a 7-story full scale reinforced concrete structural wall building slice phase II: t-wall. *SSRP.* 2007;:07–08.

62. Erazo K., Hernandez E. M.. High-resolution seismic monitoring of instrumented buildings using a model-based state observer. *Earthquake Engineering & Structural Dynamics.* 2016;45(15):2513-2531.

63. Ebrahimian M, Todorovska MI, Falborski T. Wave method for structural health monitoring: testing using full-scale shake table experiment data. *Journal of Structural Engineering.* 2016;143(4):04016217.

64. Moaveni Babak, He Xianfei, Conte Joel P, Restrepo José I, Panagiotou Marios. System identification study of a 7-story full-scale building slice tested on the UCSD-NEES shake table. *Journal of Structural Engineering.* 2010;137(6):705–717.

65. Moaveni Babak, He Xianfei, Conte Joel P, Restrepo Jose I. Damage identification study of a seven-story full-scale building slice tested on the UCSD-NEES shake table. *Structural Safety.* 2010;32(5):347–356.

66. Simoen Ellen, Moaveni Babak, Conte Joel P, Lombaert Geert. Uncertainty quantification in the assessment of progressive damage in a 7-story full-scale building slice. *Journal of Engineering Mechanics.* 2013;139(12):1818–1830.

67. Moaveni Babak, Barbosa Andre R, Conte Joel P, Hemez François M. Uncertainty analysis of system identification results obtained for a seven-story building slice tested on the UCSD-NEES shake table. *Structural Control and Health Monitoring.* 2014;21(4):466–483.

68. Moaveni Babak, Conte Joel P. *System and damage identification of civil structures*. Springer; 2007.

69. Sun Hao, Büyüköztürk Oral. The MIT Green Building benchmark problem for structural health monitoring of tall buildings. *Structural Control and Health Monitoring.* 2018;25(3):e2115.

70. Beck Robert Teran. Fundamental problems in the application of structural identification procedures to damage detection. 1991;.

71. Pandey AK, Biswas M, Samman MM. Damage detection from changes in curvature mode shapes. *Journal of sound and vibration.* 1991;145(2):321–332.

72. Vanik Michael W, Beck James L, Au SK2000. Bayesian probabilistic approach to structural health monitoring. *Journal of Engineering Mechanics.* 2000;126(7):738–745.

73. Yuen Ka-Veng. *Bayesian methods for structural dynamics and civil engineering*. John Wiley & Sons; 2010.

74. Ghanem Roger, Shinozuka Masanobu. Structural-system identification. I: Theory. *Journal of Engineering Mechanics.* 1995;121(2):255–264.

75. Sohn Hoon, Farrar Charles R. Damage diagnosis using time series analysis of vibration signals. *Smart materials and structures.* 2001;10(3):446.

76. Liu Shih-Chi, Tomizuka Masayoshi, Ulsoy Galip. Strategic issues in sensors and smart structures. *Structural Control and Health Monitoring.* 2006;13(6):946–957.

77. Ljung Lennart. System identification. In: Springer 1998 (pp. 163–173).

78. Michelson Albert A, Morley Edward W. On the Relative Motion of the Earth and of the Luminiferous Ether. *Sidereal Messenger, vol. 6, pp. 306-310.* 1887;6:306–310.

79. Abbott BP, Abbott R, Adhikari R, et al. LIGO: the laser interferometer gravitational-wave observatory. *Reports on Progress in Physics.* 2009;72(7):076901.

80. Curtis Andrew, Gerstoft Peter, Sato Haruo, Snieder Roel, Wapenaar Kees. Seismic interferometry?Turning noise into signal. *The Leading Edge.* 2006;25(9):1082–1092.

81. Wapenaar Kees, Draganov Deyan, Snieder Roel, Campman Xander, Verdel Arie. Tutorial on seismic interferometry: Part 1?Basic principles and applications. *Geophysics.* 2010;75(5):75A195–75A209.

82. Todorovska MI, Trifunac MD. Propagation of earthquake waves in buildings with soft first floor. *Journal of Engineering Mechanics.* 1990;116(4):892–900.

83. Wegler U, Nakahara H, Sens-Schönfelder C, Korn M, Shiomi K. Sudden drop of seismic velocity after the 2004 Mw 6.6 mid-Niigata earthquake, Japan, observed with passive image interferometry. *Journal of Geophysical Research: Solid Earth.* 2009;114(B6).

84. Bathe Klaus-Jürgen. *Finite element procedures*. Klaus-Jurgen Bathe; 2006.

85. De Finetti Bruno. *Theory of Probability: A Critical Introductory Treatment. Transl. by Antonio Machi and Adrian Smith*. J. Wiley; 1974.

86. Peterka V. Bayesian approach to system identification. *Trends and Progress in System identification.* 1981;1:239–304.

87. Hastings W Keith. Monte Carlo sampling methods using Markov chains and their applications. *Biometrika.* 1970;57(1):97–109.

88. Metropolis Nicholas, Rosenbluth Arianna W, Rosenbluth Marshall N, Teller Augusta H, Teller Edward. Equation of state calculations by fast computing machines. *The journal of chemical physics.* 1953;21(6):1087–1092.

89. Yuen Ka-Veng, Beck James L, Katafygiotis Lambros S. Efficient model updating and health monitoring methodology using incomplete modal data without mode matching. *Structural Control and Health Monitoring.* 2006;13(1):91–107.

90. Green PL. Bayesian system identification of a nonlinear dynamical system using a novel variant of simulated annealing. *Mechanical Systems and Signal Processing.* 2015;52:133–146.

91. D'Agostini Giulio. *Bayesian reasoning in data analysis: A critical introduction*. World Scientific; 2003.

92. Jaynes Edwin T. Information theory and statistical mechanics. *Physical review.* 1957;106(4):620.

93. MacKay David JC. *Information theory, inference and learning algorithms*. Cambridge university press; 2003.

94. Ching Jianye, Muto Matthew, Beck James L. Structural model updating and health monitoring with incomplete modal data using Gibbs sampler. *Computer-Aided Civil and Infrastructure Engineering.* 2006;21(4):242–257.

95. Liu Ce, Torralba Antonio, Freeman William T., Durand Frédo, Adelson Edward H.. Motion magnification. *ACM Trans. Graph.*. 2005;24:519–526.

96. Wu Hao-Yu, Rubinstein Michael, Shih Eugene, Guttag John, Durand Frédo, Freeman William. Eulerian Video Magnification for Revealing Subtle Changes in the World. *ACM Trans. Graph. (Proc. SIGGRAPH).* 2012;31.

97. Wadhwa Neal, Rubinstein Michael, Durand Frédo, Freeman William T. Phase-based video motion processing. *ACM Transactions on Graphics (TOG).* 2013;32(4):80.

98. Wadhwa Neal, Rubinstein Michael, Durand Frédo, Freeman William T. Riesz Pyramid for Fast Phase-Based Video Magnification. In: IEEE; 2014.

99. Davis Abe, Chen Justin G, Durand Frédo. Image-space modal bases for plausible manipulation of objects in video. *ACM Transactions on Graphics (TOG).* 2015;34(6):239.

100. Davis Abe, Rubinstein Michael, Wadhwa Neal, Mysore Gautham, Durand Fredo, Freeman William T.. The Visual Microphone: Passive Recovery of Sound from Video. *ACM Transactions on Graphics (Proc. SIGGRAPH).* 2014;33(4):79:1–79:10.

101. Rubinstein Michael. Analysis and Visualization of Temporal Variations in Video. PhD thesisMassachusetts Institute of Technology2014.

102. Davis* Abe, Bouman* Katherine L, Chen Justin G, Rubinstein Michael, Durand Frédo, Freeman William T. Visual vibrometry: Estimating material properties from small motions in video. In: :5335–5343IEEE; 2015. *Joint first author.

103. Wadhwa Neal. Revealing and Analyzing Imperceptible Deviations in Images and Videos. PhD thesisMassachusetts Institute of Technology2016.

104. Wadhwa Neal, Dekel Tali, Wei Donglai, Durand Frédo, Freeman William T. Deviation magnification: revealing departures from ideal geometries. *ACM Transactions on Graphics (TOG).* 2015;34(6):226.

105. Dekel Tali, Michaeli Tomer, Irani Michal, Freeman William T. Revealing and modifying non-local variations in a single image. *ACM Transactions on Graphics (TOG).* 2015;34(6):227.